IDŐJÁRÁS

QUARTERLY JOURNAL
OF THE HUNGARIAN METEOROLOGICAL SERVICE

CONTENTS

****

http://www.met.hu/Journal-Idojaras.php

VOL. 111 * NO. 1 * JANUARY – MARCH 2007

IDŐJÁRÁS

Quarterly Journal of the Hungarian Meteorological Service

Editorial Office: P.O. Box 39, H-1675 Budapest, Hungary or
Gilice tér 39, H-1181 Budapest, Hungary
E-mail: bozo.l@met.hu or *antal.e@met.hu*
Fax: (36-1) 346-4809

Subscription by

mail: IDŐJÁRÁS, P.O. Box 39, H-1675 Budapest, Hungary;
E-mail: bozo.l@met.hu or *antal.e@met.hu*; *Fax: (36-1) 346-4809*

IDŐJÁRÁS

Quarterly Journal of the Hungarian Meteorological Service
Vol. 111, No. 1, January–March 2007, pp. 1–40

Greenhouse effect in semi-transparent planetary atmospheres

Ferenc M. Miskolczi

Holston Lane 3, Hampton VA 23664, U.S.A.
E-mail: fmiskolczi@cox.net

(Manuscript received in final form October 29, 2006)

Abstract—In this work the theoretical relationship between the clear-sky outgoing infrared radiation and the surface upward radiative flux is explored by using a realistic finite semi-transparent atmospheric model. We show that the fundamental relationship between the optical depth and source function contains real boundary condition parameters. We also show that the radiative equilibrium is controlled by a special atmospheric transfer function and requires the continuity of the temperature at the ground surface. The long standing misinterpretation of the classic semi-infinite Eddington solution has been resolved. Compared to the semi-infinite model, the finite semi-transparent model predicts much smaller ground surface temperature and a larger surface air temperature. The new equation proves that the classic solution significantly overestimates the sensitivity of greenhouse forcing to optical depth perturbations. In Earth-type atmospheres sustained planetary greenhouse effect with a stable ground surface temperature can only exist at a particular planetary average flux optical depth of 1.841. Simulation results show that the Earth maintains a controlled greenhouse effect with a global average optical depth kept close to this critical value. The broadband radiative transfer in the clear Martian atmosphere follows different principle resulting in different analytical relationships among the fluxes. Applying the virial theorem to the radiative balance equation, we present a coherent picture of the planetary greenhouse effect.

Key-words: greenhouse effect, radiative equilibrium

1. Introduction

Recently, using powerful computers, virtually any atmospheric radiative transfer problem can be solved by numerical methods with the desired accuracy without using extensive approximations and complicated mathematical expressions common in the literature of the theoretical radiative

transfer. However, to improve the understanding of the radiative transfer processes, it is sometimes useful to apply reasonable approximations and to arrive at solutions in more or less closed mathematical forms which clearly reflect the physics of the problem.

Regarding the planetary greenhouse effect, one must relate the amount of the atmospheric infrared (IR) absorbers to the surface temperature and the total absorbed short wave (SW) radiation. In this paper we derive purely theoretical relationships between the above quantities by using a simplified one dimensional atmospheric radiative transfer model. The relationships among the broadband atmospheric IR fluxes at the boundaries are based on the flux optical depth. The atmospheric total IR flux optical depths are obtained from sophisticated high-resolution spectral radiative transfer computations.

2. Radiative transfer model

In *Fig. 1* our semi-transparent clear sky planetary atmospheric model and the relevant (global mean) radiative flux terms are presented.

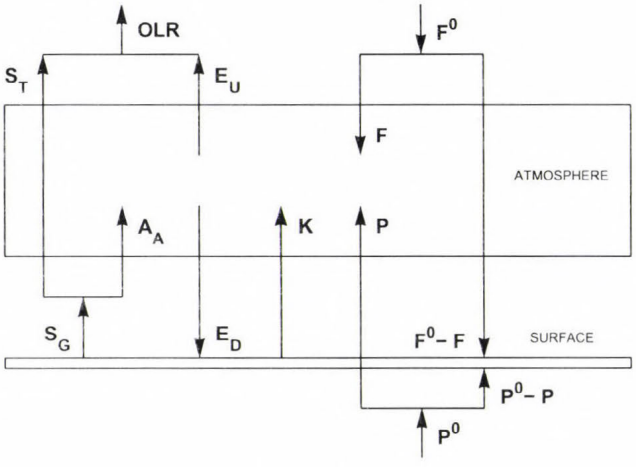

Fig. 1. Radiative flux components in a semi-transparent clear planetary atmosphere. Short wave downward: F^0 and F; long wave downward: E_D; long wave upward: OLR, E_U, S_T, A_A, and S_G; non-radiative origin: K, P^0 and P.

Here F^0 is the total absorbed SW radiation in the system, F is the part of F^0 absorbed within the atmosphere, E_D is the long wave (LW) downward atmospheric radiation, OLR is the outgoing LW radiation, E_U is the LW

upward atmospheric radiation. S_G is the LW upward radiation from the ground: $S_G = \sigma t_G^4$, where t_G is the ground temperature and σ is the Stefan-Boltzmann constant. S_T and A_A are the transmitted and absorbed parts of S_G, respectively. The total thermal energy from the planetary interior to the surface-atmosphere system is P^0. P is the absorbed part of P^0 in the atmosphere. The net thermal energy to the atmosphere of non-radiative origin is K. The usual measure of the clear-sky atmospheric greenhouse effect is the $G = S_G - OLR$ greenhouse factor (*Inamdar* and *Ramanathan*, 1997). The normalized greenhouse factor is defined as the $G_N = G/S_G$ ratio. In some work the S_G/OLR ratio is also used as greenhouse parameter (*Stephens et al.*, 1993).

Our model assumptions are quite simple and general:

(a) — The available SW flux is totally absorbed in the system. In the process of thermalization F^0 is instantly converted to isotropic upward and downward LW radiation. The absorption of the SW photons and emission of the LW radiation are based on independent microphysical processes.

(b) — The temperature or source function profile is the result of the equilibrium between the IR radiation field and all other sinks and sources of thermal energy (latent heat transfer, convection, conduction, advection, turbulent mixing, short wave absorption, etc.). Note, that the K term is not restricted to strict vertical heat transfer. Due to the permanent motion of the atmosphere K represents a statistical or climatic average.

(c) — The atmosphere is in local thermodynamic equilibrium (LTE). In case of the Earth this is true up to about 60 km altitude.

(d) — The surface heat capacity is equal to zero, the surface emissivity ε_G is equal to one, and the surface radiates as a perfect blackbody.

(e) — The atmospheric IR absorption and emission are due to the molecular absorption of IR active gases. On the Earth these gases are minor atmospheric constituents. On the Mars and Venus they are the major components of the atmosphere.

(f) — In case of the Earth it is also assumed that the global average thermal flux from the planetary interior to the surface-atmosphere system is negligible, $P^0 = 0$. The estimated geothermal flux at the surface is less than 0.03 per cent of F^0 (*Peixoto* and *Oort*, 1992). However, in our definition P^0 is not

restricted to the geothermal flux. It may contain the thermal energy released into the atmosphere by volcanism, tidal friction, or by other natural and non-natural sources.

(g) — The atmosphere is a gravitationally bounded system and constrained by the virial theorem: the total kinetic energy of the system must be half of the total gravitational potential energy. The surface air temperature, t_A, is linked to the total gravitational potential energy through the surface pressure and air density. The temperature, pressure, and air density obey the gas law, therefore, in terms of radiative flux $S_A = \sigma t_A^4$ represents also the total gravitational potential energy.

(h) — In the definition of the greenhouse temperature change keeping t_A and t_G different could pose some difficulties. Since the air is in permanent physical contact with the surface, it is reasonable to assume that, in the average sense, the surface and close-to-surface air are in thermal equilibrium: $t_S = t_A = t_G$, where t_S is the equilibrium temperature. The corresponding equilibrium blackbody radiatiation is $S_U = \sigma t_S^4$. For now, in *Fig. 1* S_G is assumed to be equal to S_U.

Assumptions (c), (d), (e), and (f) are commonly applied in broadband LW flux computations, see for example in *Kiehl* and *Trenberth* (1997). Under such conditions the energy balance equation of the atmosphere may be written as:

$$F + P + K + A_A - E_D - E_U = 0. \tag{1}$$

The balance equation at the lower boundary (surface) is:

$$F^0 + P^0 + E_D - F - P - K - A_A - S_T = 0. \tag{2}$$

The sum of these two equations results in the general relationship of:

$$F^0 + P^0 = S_T + E_U = OLR. \tag{3}$$

This is a simple radiative (energy) balance equation and not related to the vertical structure of the atmosphere. For the Earth this equation simplifies to the well known relationship of $F^0 = OLR$. For long term global mean fluxes these balance equations are exact and they are the requirements for the steady-state climate. However, they do not necessarily hold for zonal or regional averages or for instantaneous local fluxes.

The most apparent reason of any zonal or local imbalance is related to the K term through the general circulation. For example, evaporation and precipitation must be balanced globally, but due to transport processes, they can add or remove optical depth to and from an individual air column in a non-balanced way. The zonal and meridional transfer of the sensible heat is another example.

When comparing clear sky simulation results of the LW fluxes, one should be careful with the cloud effects. Due to the SW effect of the cloud cover on F^0 and F, clear sky computations based on all sky radiosonde observations will also introduce deviations from the balance equations.

The true all sky outgoing LW radiation, OLR^A, must be computed from the clear OLR and the cloudy OLR^C fluxes as the weighted average by the fractional cloud cover: $OLR^A = (1-\beta)OLR + \beta OLR^C$, where β is the fractional cloud cover. Because of the large variety of cloud types and cloud cover and the required additional information on the cloud top altitude, temperature, and emissivity, the simulation of OLR^C is rather complicated.

The global average OLR^A may be estimated from the bolometric planetary equilibrium temperature. From the *ERBE* (2004) data product we estimated the five year average planetary equilibrium temperature as $t_E = 253.8$ K, which resulted in a global average $OLR^A = 235.2$ W m^{-2}. From the same data product the global average clear-sky OLR is 266.4 W m^{-2}.

3. Kirchhoff law

According to the Kirchhoff law, two systems in thermal equilibrium exchange energy by absorption and emission in equal amounts, therefore, the thermal energy of either system can not be changed. In case the atmosphere is in thermal equilibrium with the surface, we may write that:

$$A_A = S_U A = S_U (1 - T_A) = E_D . \tag{4}$$

By definition the atmospheric flux transmittance T_A is equal to the S_T / S_U ratio: $T_A = 1 - A = \exp(-\tilde{\tau}_A) = S_T / S_U$, where A is the flux absorptance and $\tilde{\tau}_A$ is the total IR flux optical depth. The validity of the Kirchhoff law – concerning the surface and the inhomogeneous atmosphere above – is not trivial. Later, using the energy minimum principle, we shall give a simple theoretical proof of the Kirchhoff law for atmospheres in radiative equilibrium.

In *Fig. 2* we present large scale simulation results of A_A and E_D for two measured diverse planetary atmospheric profile sets. Details of the simulation exercise above were reported in *Miskolczi* and *Mlynczak* (2004). This figure is

a proof that the Kirchhoff law is in effect in real atmospheres. The direct consequences of the Kirchhoff law are the next two equations:

$$E_U = F + K + P, \tag{5}$$

$$S_U - (F^0 + P^0) = E_D - E_U . \tag{6}$$

The physical interpretations of these two equations may fundamentally change the general concept of greenhouse theories.

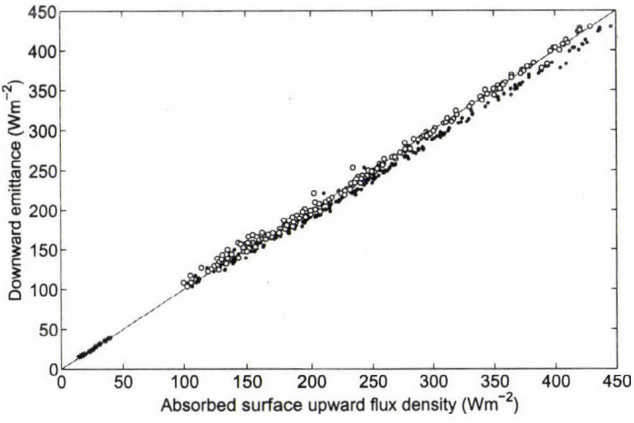

Fig. 2. Simulation results of A_A and E_D. Black dots and open circles represent 228 selected radiosonde observations with $\varepsilon_G = 1$ and $\varepsilon_G = 0.96$, respectively. Black stars are simulation results for Martian standard atmospheric profiles with $\varepsilon_G = 1$. We used two sets of eight standard profiles. One set contained no water vapor and in the other the water vapor concentration was set to constant 210 ppmv (approximately 0.0015 prcm H_2O).

3.1 Upward atmospheric radiation

Eq. (5) shows that the source of the upward atmospheric radiation is not related to LW absorption processes. The $F + K + P$ flux term is always dissipated within the atmosphere increasing (or decreasing) its total thermal energy. The $E_D = S_U - S_T$ functional relationship implies that $G - E_D = -E_U$, therefore, the interpretation of $G - E_D$ as the LW radiative heating (or cooling) of the atmosphere in *Inamdar* and *Ramanathan* (1997) could be misleading.

Regarding the origin, E_U is more closely related to the total internal kinetic energy of the atmosphere, which – according to the virial theorem – in

hydrostatic equilibrium balances the total gravitational potential energy. To identify E_U as the total internal kinetic energy of the atmosphere, the $E_U = S_U / 2$ equation must hold. E_U can also be related to G_N through the $E_U = S_U (A - G_N)$ equation. In opaque atmospheres $A = 1$ and the $G_N = 0.5$ is the theoretical upper limit of the normalized greenhouse factor.

3.2 Hydrostatic equilibrium

In Eq. (6) $S_U - (F^0 + P^0)$ and $E_D - E_U$ represent two flux terms of equal magnitude, propagating into opposite directions, while using the same F^0 and P^0 as energy sources. The first term heats the atmosphere and the second term maintains the surface energy balance. The principle of conservation of energy dictates that:

$$S_U - (F^0 + P^0) + E_D - E_U = F^0 + P^0 = OLR\,. \tag{7}$$

This equation poses a strict criterion on the global average S_U:

$$S_U = 3OLR/2 \;\rightarrow\; S_U - (F^0 + P^0) = R\,. \tag{8}$$

In the right equation R is the pressure of the thermal radiation at the ground: $R = S_U / 3$. This equation might make the impression that G does not depend on the atmospheric absorption, which is generally not true. We shall see that under special conditions this dependence is negligible. Eq. (8) expresses the conservation of radiant energy but does not account for the fact, that the atmosphere is gravitationally bounded. Implementing the virial theorem into Eq. (8) is relatively simple. In the form of an additive S_V 'virial' term we obtained the general radiative balance equation:

$$S_U + S_T/2 - E_D/10 = 3OLR/2 \;\rightarrow\; S_U - (F^0 + P^0) = 6RA/5\,. \tag{9}$$

In Eq. (9) the $S_V = S_T/2 - E_D/10$ virial term will force the hydrostatic equilibrium while maintaining the radiative balance. From Eq. (9) follow the $3/5 + 2T_A/5 = OLR/S_U$ and the $E_U/E_D = 3/5$ relations. This equation is based on the principle of the conservation of energy and the virial theorem, and we expect that it will hold for any clear absorbing planetary atmosphere.

The optimal conversion of $F^0 + P^0$ to OLR would require that either $T_A \approx 0$ or $T_A \approx 1$. The first case is a planet with a completely opaque atmophere with saturated greenhouse effect, and the second case is a planet without greenhouse gases. For the Earth obviously the $T_A \approx 0$ condition apply and the $OLR^A / S_U^A = 3/5$ equation gives an optimal global average surface

upward flux of $S_U^A = 392$ W m^{-2} and a global average surface temperature of 288.3 K. We know that – because of the existence of the IR atmospheric window – the flux transmittance must not be zero and the atmosphere can not be opaque. The Earth's atmosphere solves this contradiction by using the radiative effect of a partial cloud cover.

For atmospheres, where $E_D \approx 5 S_T$ or $T_A \approx 1/6$, Eq. (9) will take the form of Eq. (8). In optically thin atmospheres where, $E_D/10 << OLR$ or $S_T >> E_U$, Eq. (9) simplifies to:

$$S_U + S_T/2 = 3OLR/2 \quad \rightarrow \quad S_U - (F^0 + P^0) = R\,A\,. \tag{10}$$

Eq. (10) implies the $2/3 + T_A/3 = OLR/S_U$ and $E_U/E_D = 2/3$ relations. Applying this equation for the Earth's atmosphere will introduce more than 10% error in the OLR.

3.2 Transfer and greenhouse functions

The relationships between the OLR and S_U may be expressed by using the concept of the transfer function. The transfer function converts the surface upward radiation to outgoing LW radiation. It is practically the OLR/S_U ratio or the normalized OLR. The greenhouse functions are analogous to the empirical G_N factor introduced in Section 2. From Eqs. (8), (9), and (10) one may easily derive the $f^+ = 2/3$, $f^\circ = 1 - 2A/5$, and $f^* = 1 - A/3$ transfer functions, and the $g^+ = 1/3$, $g^\circ = 2A/5$, and $g^* = A/3$ greenhouse functions, respectively. The g^+, g°, and g^* greenhouse functions will always satisfy the $S_U > F^0 + P^0$ relationship, which is the basic requirement of the greenhouse effect. On the evolutionary time scale of a planet, the mass and the composition of the atmosphere together with the F^0 and P^0 fluxes may change dramatically and accordingly, the relevant radiative balance equation could change with the time and could be different for different planets.

The most interesting fact is, that in case of Eq. (8) $g^+ = R/S_U = 1/3$ does not depend on the optical depth. G will always be equal to the radiation pressure of the ideal gas, and the atmosphere will have a constant optical depth $\tilde{\tau}_A^+$ which is only dependent on the sum of the external SW and internal thermal radiative forcings. In Eqs. (9) and (10) the dependence of G on A is expected. Planets following the radiation scheme of Eq. (8) can not change their surface temperature without changing the surface pressure – total mass of the atmosphere – or the SW or thermal energy input to the system. This kind of planet should have relatively strong absorption ($T_A \approx 1/6$), and the greenhouse gases must be the minor atmospheric constituents with very small effect on the surface pressure. Earth is a planet of this kind. In the Martian

atmosphere E_U is far too small and in the Venusian atmosphere S_G is far too large to satisfy the $E_U \approx S_U/2$ condition, moreover, the atmospheric absorption on these planets significantly changes with the mass of the atmosphere – or with the surface pressure.

Our simulations show that on the Earth the global average transmitted radiative flux and downward atmospheric radiation are $S_T^E = 61$ W m^{-2} and $E_D^E = 309$ W m^{-2}. The $S_T^E \approx E_D^E/5$ approximation holds and Eq. (8) with the g^+ greenhouse function may be used. The global average clear sky S_U and OLR are $S_U^E = 382$ W m^{-2} and $OLR^E = 250$ W m^{-2}. Correcting this S_U^E to the altitude level where the OLR was computed (61.2 km), we may calculate the global average G_N as $G_N^E = (S_U^E - OLR^E)/S_U^E = 0.332$. In fact, G_N^E is in very good agreement with the theoretical $g^+ = 0.333$. The simulated global average flux optical depth is $\tilde{\tau}_A^E = -\ln(T_A^E) = 1.87$, where T_A^E is the global average flux transmittance. This simulated $\tilde{\tau}_A^E$ can not be compared with theoretical optical depths from Eq. (8) without the explicit knowledge of the $S_U(OLR, \tilde{\tau}_A)$ function. The best we can do is to use Eq. (9) – the $T_A = 1/6$ condition – to get an estimate of $\tilde{\tau}_A^+ \approx -\ln(1/6) = 1.79$, which is not very far from our $\tilde{\tau}_A^E$.

The popular explanation of the greenhouse effect as the result of the LW atmospheric absorption of the surface radiation and the surface heating by the atmospheric downward radiation is incorrect, since the involved flux terms (A_A and E_D) are always equal. The mechanism of the greenhouse effect may better be explained as the ability of a gravitationally bounded atmosphere to convert $F^0 + P^0$ to OLR in such a way that the equilibrium source function profile will assure the radiative balance ($F^0 + P^0 = OLR$), the validity of the Kirchhoff law ($E_D = S_U A$), and the hydrostatic equilibrium ($S_U = 2E_U$). Although an atmosphere may accommodate the thermal structure needed for the radiative equilibrium, it is not required for the greenhouse effect. Formally, in the presence of a solid or liquid surface, the radiation pressure of the thermalized photons is the real cause of the greenhouse effect, and its origin is related to the principle of the conservation of the momentum of the radiation field.

Long term balance between $F^0 + P^0$ and OLR can only exist at the $S_U = (F^0 + P^0)/(1 - 2A/5) \approx 3(F^0 + P^0)/2$ planetary equilibrium surface upward radiation. It worth to note that S_U does not depend directly on F, meaning that the SW absorption may happen anywhere in the system. F^0 depends only on the system albedo, the solar constant, and other relevant astronomical parameters.

In the broad sense the surface-atmosphere system is in the state of radiative balance if the radiative flux components satisfy Eqs. (3), (4), and (8). The equivalent forms of these conditions are the $E_D - E_U = S_U/3$ and $E_D - E_U = OLR/2$ equations. In such case there is no horizontal exchange of energy with the surrounding environment, and the use of a one dimensional or single-column model for global energy budget studies is justified.

Our task is to establish the theoretical relationship between S_U and OLR as the function of $\tilde{\tau}_A$ for semi-transparent bounded atmospheres assuming, that the radiative balance (Eqs. (8) and (9)) is maintained and the thermal structure (source function profile) satisfies the criterion of the radiative equilibrium. The evaluation of the response of an atmosphere for greenhouse gas perturbations is only possible with the explicit knowledge of such relationship.

4. Flux optical depth

To relate the total IR absorber amount to the flux densities, the most suitable parameter is the total IR flux optical depth. In the historical development of the gray approximation different spectrally averaged mean optical depths were introduced to deal with the different astrophysical problems (*Sagan*, 1969). If we are interested in the thermal emission, our relevant mean optical depth will be the Planck mean. Unfortunately, the Planck mean works only with very small monochromatic optical depths (*Collins*, 2003). In the Earth atmosphere the infrared monochromatic optical depth is varying many orders of magnitude, therefore, the required criteria for the application of the Planck mean is not satisfied.

This problem can be eliminated without sacrificing accuracy by using the simulated flux optical depth. Such optical depths may be computed from monochromatic directional transmittance by integrating over the hemisphere. We tuned our line-by-line (LBL) radiative transfer code (HARTCODE) for an extreme numerical accuracy, and we were able to compute the flux optical depth in a spherical refractive environment with an accuracy of five significant digits (*Miskolczi et al.*, 1990). To obtain this accuracy 9 streams, 150 homogeneous vertical layers, and 1 cm^{-1} spectral resolution were applied. These criteria control the accuracy of the numerical hemispheric and altitude integration and the convolution integral with the blackbody function, see Appendix A.

All over this paper the simulated total flux optical depths were computed as the negative natural logarithms of these high accuracy Planck weighted hemispheric monochromatic transmittance: $\tilde{\tau}_A = -\ln(T_A)$.

In a non-scattering atmosphere, theoretically, the dependence of the source function on the monochromatic optical depth is the solution of the following differential equation (*Goody* and *Young*, 1989):

$$\frac{d^2 H_\nu(\tau_\nu)}{d\tau_\nu^2} - 3H_\nu(\tau_\nu) = -4\pi \frac{dJ_\nu(\tau_\nu)}{d\tau_\nu}, \tag{11}$$

where $H_\nu(\tau_\nu)$ is the monochromatic net radiative flux (Eddington flux) and $J_\nu(\tau_\nu)$ is the monochromatic source function, which is – in LTE – identical with the Planck function, $J_\nu(\tau_\nu) = B_\nu(\tau_\nu)$. The vertically measured monochromatic optical depth is τ_ν. Eq. (11) assumes the isotropy of the radiation field in each hemisphere and the validity of the Eddington approximation.

For monochromatic radiative equilibrium $dH_\nu(\tau_\nu)/d\tau_\nu = 0$ and Eq. (11) becomes a first order linear differential equation for $B_\nu(\tau_\nu)$. Applying the gray approximation, one finds that there will be no dependence on the wave number, τ_ν will become a mean vertical gray-body optical depth, $\overline{\tau}$, and H will become the net radiative flux:

$$dB(\overline{\tau})/d\overline{\tau} = 3H/(4\pi). \tag{12}$$

The well known solution of Eq. (12) is:

$$B(\overline{\tau}) = (3/4\pi)H\overline{\tau} + B_0. \tag{13}$$

According to Eq. (13), in radiative equilibrium the source function increases linearly with the gray-body optical depth. The integration constant, B_0, can be determined from the Schwarzschild-Milne equation, which relates the net flux to the differences in the hemispheric mean intensities:

$$H(\overline{\tau}) = \pi(\overline{I}^+ - \overline{I}^-), \tag{14}$$

where $\overline{I}^+$ and $\overline{I}^-$ are the upward and downward hemispheric mean intensities, respectively. In the solution of Eq. (12) one has to apply the appropriate boundary conditions. In the further discussion we shall allow S_G and S_A to be different.

4.1 Semi-infinite atmosphere

In the semi-infinite atmosphere, the total vertical optical depth of the atmosphere is infinite. The boundary condition is usually given at the top of the atmosphere, where, due to the absence of the downward flux term, the net IR flux is known. Using the general classic solutions of the plane-parallel radiative transfer equation in Eq. (14), one sees that the integration constant will become $B_0 = H/(2\pi)$. Putting this B_0 into Eq. (13) will generate the classic semi-infinite solution for the $B(\tilde{\tau})$ source function:

$$B(\tilde{\tau}) = H(1+\tilde{\tau})/(2\pi), \tag{15}$$

where $\tilde{\tau}$ is the flux optical depth, as usually defined in two stream approximations, $\tilde{\tau} = (3/2)\bar{\tau}$. In astrophysics monographs Eq. (15) is referred to as the solution of the Schwarzschild-Milne type equation for the gray atmosphere using the Eddington approximation.

The characteristic gray-body optical depth, $\hat{\tau}_C$, defines the IR optical surface of the atmosphere: $\pi B(\hat{\tau}_C) = H$. The 'hat' indicates that this is a theoretically computed quantity. At the upper boundary, $\tilde{\tau} = 0$, the source function is finite, and is usually associated with the atmospheric skin temperature: $\pi B_0 = \pi B(0) = H/2$. Note, that in obtaining B_0, the fact of the semi-infinite integration domain over the optical depth in the formal solution is widely used. For finite or optically thin atmosphere Eq. (15) is not valid. In other words, this equation does not contain the necessary boundary condition parameters for the finite atmosphere problem.

Despite the above fact, in the literature of atmospheric radiation and greenhouse effect, Eq. (15) is almost exclusively applied to derive the dependence of the surface air temperature and the ground temperature on the total flux optical depth (*Goody* and *Yung*, 1989; *Stephens* and *Greenwald*, 1991; *McKay et al.*, 1999; *Lorenz* and *McKay*, 2003):

$$t_A^4 = t_E^4(1 + \tilde{\tau}_A)/2, \tag{16}$$

$$t_G^4 = t_E^4(2 + \tilde{\tau}_A)/2, \tag{17}$$

where $t_A^4 = \pi B(\tilde{\tau}_A)/\sigma$, $t_G^4 = t_A^4 + t_E^4/2$, and $t_E^4 = H/\sigma = OLR/\sigma$ are the surface air temperature, ground temperature, and the effective temperature, respectively. At the top of the atmosphere the net IR radiative flux is equal to the global average outgoing long wave radiation. As we have already seen, when long term global radiative balance exists between the SW and LW radiation, OLR is equal to the sum of the global averages of the available SW solar flux and the heat flux from the planetary interior.

Eq. (15) assumes that at the lower boundary the total flux optical depth is infinite. Therefore, in cases, where a significant amount of surface transmitted radiative flux is present in the OLR, Eqs. (16) and (17) are inherently incorrect. In stellar atmospheres, where, within a relatively short distance from the surface of a star the optical depth grows tremendously, this could be a reasonable assumption, and Eq. (15) has great practical value in astrophysical applications. The semi-infinite solution is useful, because there is no need to specify any explicit lower boundary temperature or radiative flux parameter (*Eddington*, 1916).

When considering the clear-sky greenhouse effect in the Earth's atmosphere or in optically thin planetary atmospheres, Eq. (16) is physically

meaningless, since we know that the *OLR* is dependent on the surface temperature, which conflicts with the semi-infinite assumption that $\tilde{\tau}_A = \infty$. Eq. (17) is also not a prescribed mathematical necessity, but an incorrect assumption for the downward atmospheric radiation and applying the relationship of Eq. (16). As a consequence, Eq. (16) will underestimate t_A, and Eq. (17) will largely overestimate t_G (*Miskolczi* and *Mlynczak*, 2004).

There were several attempts to resolve the above deficiencies by developing simple semi-empirical spectral models, see for example *Weaver* and *Ramanathan* (1995), but the fundamental theoretical problem was never resolved. The source of this inconsistency can be traced back to several decades ago, when the semi-infinite solution was first used to solve bounded atmosphere problems. About 80 years ago Milne stated: "Assumption of infinite thickness involves little or no loss of generality", and later, in the same paper, he created the concept of a secondary (internal) boundary (*Milne*, 1922). He did not realize that the classic Eddington solution is not the general solution of the bounded atmosphere problem and he did not re-compute the appropriate integration constant. This is the reason why scientists have problems with a mysterious surface temperature discontinuity and unphysical solutions, as in *Lorenz* and *McKay* (2003). To accommodate the finite flux optical depth of the atmosphere and the existence of the transmitted radiative flux from the surface, the proper equations must be derived.

4.2 Bounded atmosphere

In the bounded or semi-transparent atmosphere $OLR = E_U + S_T$. In the Earth's atmosphere, the lower boundary conditions are well defined and explicitly given by t_A, t_G, and $\tilde{\tau}_A$. The surface upward hemispheric mean radiance is $B_G = S_G / \pi = \sigma t_G^4 / \pi$. The upper boundary condition at the top of the atmosphere is the zero downward IR radiance.

The complete solution of Eq. (12) requires only one boundary condition. To evaluate B_0 we can use either the top of the atmosphere or the surface boundary conditions since both of them are defined. Applying the boundary conditions in Eq. (14) at $H = H(0)$ and $H = H(\overline{\tau}_A)$ will yield two different equations for B_0. The traditional way is to solve this as a system of two independent equations for B_0 and B_G as unknowns, and arrive at the semi-infinite solution with a prescribed temperature discontinuity at the ground. In the traditional way, therefore, B_G becomes a constant, which does not represent the true lower boundary condition.

The source of the problem is, that at the lower boundary B_G is treated as an arbitrary parameter. In reality, when considering the Schwarzschild-Milne equation at $H = H(\overline{\tau}_A)$, we must apply a constraint for B_G. In the introduction

we showed that this is set by the total energy balance requirement of the system: $OLR = S_G - E_D + E_U$. Using the above condition for solving Eq. (14) at $H = H(\bar{\tau}_A)$ will be equivalent to solving the same equation at $H = H(0)$. For mathematical simplicity now we introduce the atmospheric transfer and greenhouse functions by the following definitions:

$$f(\tilde{\tau}_A) = 2/(1 + \tilde{\tau}_A + \exp(-\tilde{\tau}_A)), \tag{18}$$

and

$$g(\tilde{\tau}_A) = (\tilde{\tau}_A + \exp(-\tilde{\tau}_A) - 1)/(\tilde{\tau}_A + \exp(-\tilde{\tau}_A) + 1). \tag{19}$$

The f and g are special functions and they have some useful mathematical properties: $f = 1 - g$ and $dg/d\tilde{\tau}_A = -df/d\bar{\tau}_A = f^2 A/2$. Later we shall see that in case of radiative equilibrium, these functions partition the surface upward radiative flux into the OLR and $S_G - OLR$ parts. Using the above notations the derived B_0 takes the form:

$$\pi B_0 = \frac{H}{2A}\left[\frac{2}{f} - \tilde{\tau}_A A\right] - \pi B_G T_A / A. \tag{20}$$

For large $\tilde{\tau}_A$ this B_0 tends to the semi-infinite solution. Combining Eq. (20) with Eq. (13) we obtain the general form of the source function for the bounded atmosphere:

$$\pi B(\tilde{\tau}) = \frac{H}{2A}\left[\frac{2}{f} - (\tilde{\tau} - \tilde{\tau}_A)A\right] - \pi B_G T_A / A. \tag{21}$$

We call Eq. (21) the general greenhouse equation. It gives the fundamental relationship between $\tilde{\tau}$, $\tilde{\tau}_A$, B_G, H, and the IR radiation fluxes, and this is the equation that links the surface temperatures to the column density of absorber. This equation is general in the sense, that it contains the general boundary conditions of the semi-transparent atmosphere, and asymptotically includes the classic semi-infinite solution. For the validity of Eq. (21) the radiative equilibrium condition (Eq. (12)) must hold.

We could not find any references to the above equation in the meteorological literature or in basic astrophysical monographs, however, the importance of this equation is obvious, and its application in modeling the greenhouse effect in planetary atmospheres may have far reaching consequences.

For example, radiative-convective models usually assume that the surface upward convective flux is due to the temperature discontinuity at the surface. The fact, that the new B_0 (skin temperature) changes with the surface temperature and total optical depth, can seriously alter the convective flux

estimates of previous radiative-convective model computations. Mathematical details on obtaining Eqs. (20) and (21) are summarized in Appendix B.

At the upper boundary $H = OLR$, and it is immediately clear that for large $\tilde{\tau}_A$ Eq. (21) converges to the semi-infinite case of Eq. (15). It is also clear that the frequently mentioned temperature discontinuity requirement at the surface has been removed by the explicit dependence of $B(\tilde{\tau})$ on B_G. The derivative of this equation is constant and equal to $3H/(4\pi)$, just like in the semi-infinite case, as it should be. According to Eq. (21), the surface air temperature and the characteristic optical depth depend on B_G and $\tilde{\tau}_A$:

$$\pi B(\tilde{\tau}_A) = (OLR/f - \pi B_G T_A)/A, \tag{22}$$

$$\hat{\tau}_C = 1 + \frac{2(1 - \pi B_G / OLR) + \tilde{\tau}_A}{1 - \exp(\tilde{\tau}_A)}. \tag{23}$$

Particularly simple forms of the OLR and E_U may be derived from Eq. (22):

$$OLR = f(S_A A + S_G T_A), \tag{24}$$

$$E_U = f S_A A - g S_G T_A. \tag{25}$$

In Eqs. (24) and (25) $S_A = \pi B(\tilde{\tau}_A) = \sigma t_A^4$. The upward atmospheric radiation clearly depends on the ground temperature and can not be computed without the explicit knowledge of S_G.

5. Temperature discontinuity

Now we shall again assume the thermal equilibrium at the surface: $t_S = t_A = t_G$. Inevitably, because the radiating ground surface is not a perfect blackbody, $S_U = S_A > S_G$, and $S_G = \varepsilon_G \sigma t_G^4 = \varepsilon_G \sigma t_S^4 = \varepsilon_G S_U$. From Eq. (24) one may easily express t_S:

$$t_S^4 = t_E^4 / (1 + T_A(\varepsilon_G - 1))/f. \tag{26}$$

For high emissivity and opaque areas the following approximations will hold:

$$t_S^4 = t_E^4 / f, \tag{27}$$

$$S_U = OLR/f. \tag{28}$$

The $E_U / S_U = (OLR - S_T)/S_U = f - T_A$ relationship follows from Eq. (28). This function (normalized upward atmospheric radiation) has a sharp maximum at $\tilde{\tau}_A^U = 1.59$. It is worth noting, that in Eq. (26) the dependence of t_S on ε_G opens up a greenhouse feedback channel which might have importance in relatively transparent areas with low emissivity, for example at ice covered polar regions. Also, Eq. (26) must be the preferred equation to study radiative transfer above cloud layers. Assuming the global averages of $\varepsilon_G = 0.95$ and $T_A = 0.17$, Eq. (27) will underestimate t_S by about 0.9 per cent.

So far at the definition of ε_G we ignored the reflected part of the downward long-wave flux. The true surface emissivity is: $\varepsilon'_G = E_D T_A / (S_U - E_D)/A$. ε'_G may be obtained from ε_G by applying the next correction: $\varepsilon'_G = \varepsilon_G T_A / (1 - \varepsilon_G A)$. The energy balance at the boundary is maintained by the net sensible and latent heat fluxes and other energy transport processes of non-radiative origin. Further on we shall assume that the $\varepsilon_G = \varepsilon'_G = 1$ approximation and Eqs. (27) and (28) are valid. Let us emphasize again, that these equations assume the thermal equilibrium at the ground.

5.1 Energy minimum principle

We may also arrive at Eq. (28) from a rather different route. The principle of minimum energy requires the most efficient disposal of the thermal energy of the atmosphere. Since in radiative equilibrium the quantity πB_0 is an additive constant to the source function, for a given OLR and S_G we may assume that in the atmosphere the total absorber amount (water vapor) will maximize B_0.

Mathematically, $\tilde{\tau}_A$ is set by the $dB_0 / d\tilde{\tau}_A = 0$ condition. It can be shown that this is equivalent to solve the $S_G = OLR / f$ transcendental equation for $\tilde{\tau}_A$, see the details in Appendix B. Comparing this equation with Eq. (28) follows the $S_G = S_U$ equation.

In other words, in radiative equilibrium there is a thermal equilibrium at the ground and the quantities S_G, OLR, and $\tilde{\tau}_A$ are linked together in such a way that $\tilde{\tau}_A$ will maximize B_0. The above concept is presented in *Fig. 3*. Here we show three πB_0 functions, with short vertical lines indicating the positions of their maxima. The thick solid curve was computed from Eq. (20) with the clear sky global averages of $OLR = 250\,\mathrm{W\ m^{-2}}$ and $\pi B_G = 382\ \mathrm{W\ m^{-2}}$. The open circle at $\tilde{\tau}_A = 1.87$ represents the global average πB_0 of 228 simulations.

The position of the maximum of this curve is practically coincidental with the global average $\tilde{\tau}_A^E$. The location of the maximum may be used in a parameterized $H_2O(\tilde{\tau}_A)$ function for the purely theoretical estimate of the global average water vapor content. In such estimate our global average $\tilde{\tau}_A$ would result in about 2.61 precipitable centimeter (prcm) H_2O column amount.

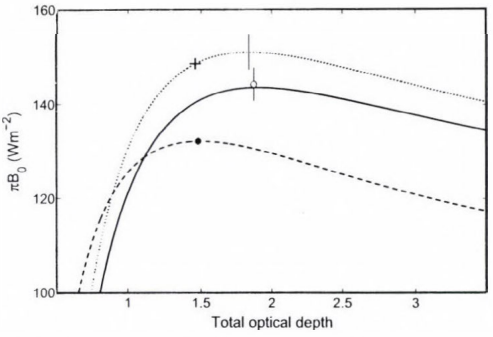

Fig. 3. $\pi B_0(\tilde{\tau}_A)$ functions computed from Eq. (20) for a realistic range of $\tilde{\tau}_A$. The solid line represents the clear-sky global average. The maximum of this curve is $\pi B_0 = 142$ W m^{-2} at $\tilde{\tau}_A = 1.86$. The open circle at $\pi B_0 = 143$ W m^{-2} and $\tilde{\tau}_A = 1.87$ is the global average of large scale line-by-line simulations involving 228 temperature and humidity profiles from around the globe. The broken line and the solid dot were computed for a zonal average arctic profile. The dotted line and the '+' symbol represent similar computations for the USST-76 atmosphere.

The broken line and the full circle show similar computations for a zonal mean arctic profile. For reference, the $\pi B_0(\tilde{\tau}_A)$ function of the U.S. Standard Atmosphere, 1976 (USST-76) is also plotted with a dotted line. In this case the actual optical depth $\tilde{\tau}_A^{US} = 1.462$ (indicated by the '+' symbol) is not coincidental with the position of tche maximum of the $\pi B_0(\tilde{\tau}_A)$ curve, meaning that this profile does not satisfy Eq. (28). Compared to the required equilibrium surface temperature of $t_A^{US} = 280.56$ K, the USST-76 atmosphere is warmer by about 7.6 K at the ground. Some further comparisons of the theoretical and simulated total optical depths are shown in *Fig. 4*.

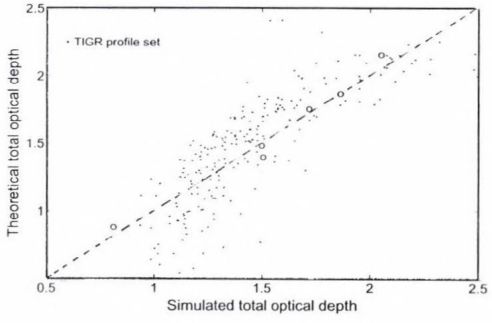

Fig. 4. Comparisons of the theoretical and simulated total flux optical depths. The inner four circles were computed for global and zonal mean temperature profiles, the leftmost circle were computed for an extremely cold arctic profile, the rightmost circle represents a mid-latitudinal summer profile. The dots show the results of 228 LBL simulations. The scatter of the dots are due to the fact that the temperature profiles were not in perfectradiative equilibrium.

The simulated data points were obtained by LBL computations using zonal mean temperature profiles at different polar and equatorial belts. The theoretical values – the solutions of Eq. (28) – are in fairly good agreement with the simulated $\tilde{\tau}_A$, the correlation coefficient is 0.989. The major conclusion of *Figs. 3* and *4* is the fact that for large scale spatial averages the finite atmosphere problem may be handled correctly with the different forms of Eqs. (24) or (28). For local or instantaneous fluxes (represented by the gray dots) the new equations do not apply because the chances to find an air column in radiative balance are slim.

5.2 Global average profiles

In *Fig. 5* we present our global average source function profile – which was computed from selected all-sky radiosonde observations – and the theoretical predictions of the semi-infinite and semi-transparent approximations.

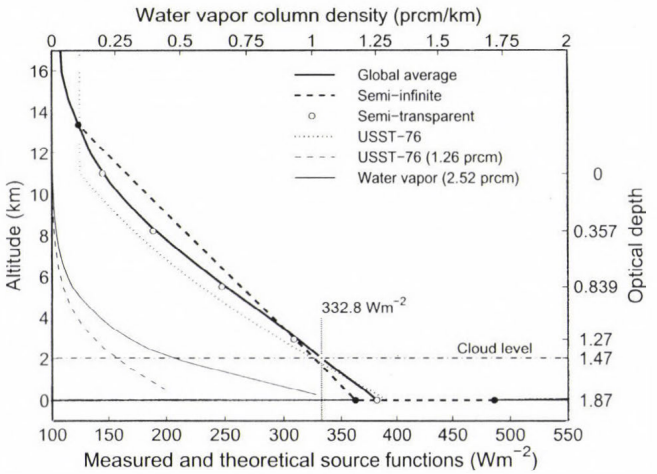

Fig. 5. Theoretical and measured source function profiles, and the global average H_2O profile. The solid lines were computed from 228 selected all sky radiosonde observations. The black dots and the dashed line represent the semi-infinite approximation with the temperature discontinuity at the ground. The open circles were computed from Eq. (21). The optical depth values of 0.357, 0.839, 1.28, 1.47, and 1.87 correspond to $\hat{\tau}_{E_1}$, $\hat{\tau}_C$, $\hat{\tau}_{E_D}$, $\tilde{\tau}_A^C \approx \tilde{\tau}_A^{US}$, and $\tilde{\tau}_A^E$, respectively. The dash-dot line is the approximate altitude of an assumed cloud layer where the $OLR^{\uparrow} = E_D = OLR$.

The source function profile of the USST-76 model atmosphere is also plotted with a dotted line. The global average tropospheric source function profile is apparently a radiative equilibrium profile satisfying Eq. (21) or the

$B(\tilde{\tau}) = OLR\,\tilde{\tau}/2 + B_0$ equation, where $B_0 = 146$ W m^{-2}. Up to 10 km altitude the $B(z) \approx OLR^A\,(1 - z/10) + B_0$ approximation may be used, where the global average OLR^A is: $OLR^A \approx OLR\,\tilde{\tau}_A^E/2$.

Clearly the new equations give a far better representation of the true average tropospheric source function profile than the one obtained from the opaque semi-infinite equation. Our source function profile corresponds to a temperature profile with an average tropospheric lapse rate of 5.41 K km^{-1}. The flux densities S_U^E and OLR^E with $\tilde{\tau}_A^E$ closely satisfy Eqs. (8), (9), and (28). This optical depth is consistent with the observed global average water vapor column amount of about 2.5 prcm in *Peixoto* and *Oort* (1992).

In *Fig. 5* the thin solid and broken lines – and the top axis – show the water vapor column density profiles of our global average and the USST-76 atmospheres respectively.

Since the Earth-atmosphere system must have a way to reduce the clear sky OLR^E to the observed OLR^A we assume the existence of an effective cloud layer at about 2.05 km altitude. The corresponding optical depth is $\tilde{\tau}_A^C = 1.47$. *Fig. 6* shows the dependences of the OLR and E_D on the cloud top altitude and E_U on the cloud bottom altitude. At this cloud level the source function is $S^C = 332.8$ W m^{-2}. We also assume that the cloud layer is in thermal equilibrium with the surrounding air and radiates as a perfect blackbody. Clear sky simulations show that at this level the $OLR \approx OLR^A \approx E_D$ and the layer is close to the radiative equilibrium. Cloudy computations also show that E_U – and consequently K – has a maximum around this level, which is favorable for cloud formation.

In cloudy areas the system loses the thermal energy to space at a rate of OLR^A which is now covered by the absorbed SW flux in the cloudy atmosphere. According to the Kirchhoff law, the downward radiation to the cloud top is also balanced. Below the cloud layer, the net LW flux is close to zero. Clouds at around 2 km altitude have minimal effect on the LW energy balance, and they seem to regulate the SW absorption of the system by adjusting the effective cloud cover β.

The $OLR^A - 2S_U^E/3 \approx -15$ W m^{-2} is a fairly good estimate of the global average cloud forcing. The estimated $\beta \approx 0.6$ is the required cloud cover (at this level) to balance OLR^A, which looks realistic. We believe that the β parameter is governed by the maximum entropy principle, the system tries to convert as much SW radiation to LW radiation as possible, while obeying the $2OLR/(3f) = F^0 + P^0$ condition. The cloud altitude, where the clear-sky $OLR = OLR^A = E_D$ depends only on the SW characteristics of the system (surface and cloud albedo, SW solar input) and alone, is a very important climate parameter.

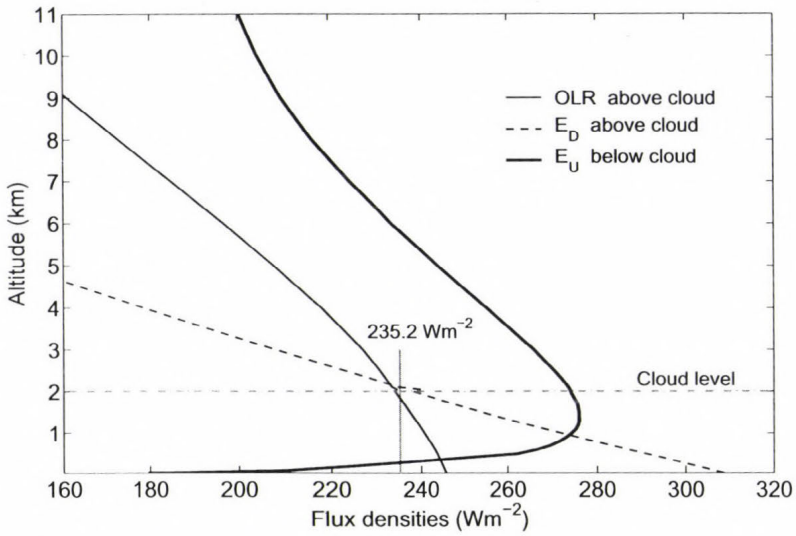

Fig. 6. Cloudy simulation results using the global average temperature and water vapor profiles. For the OLR and E_D curves the altitude is the cloud-top level. For the E_U curve the altitude is the level of the cloud-bottom. Simulations were performed at eleven cloud levels between the 0 and 11 km altitudes. The gray vertical line is the all-sky OLR^A.

In *Kiehl* and *Trenberth* (1997) the USST-76 atmosphere was used for the estimation of the clear-sky global mean E_D and OLR. To make their computed OLR consistent with the ERBE clear-sky observations, they reduced the tropospheric water vapor amount by 12%, to about 1.26 prcm. Our LBL simulation using the same profile indicates that $\tilde{\tau}_A^{US}$=1.462 and $f(\tilde{\tau}_A^{US})=0.742$, and as we have seen already, Eq. (28) is not satisfied. The expected equilibrium transfer function is $f=260.8/391.1=0.6668$, which corresponds to a global average water vapor column amount of 2.5 prcm. This value is about double of the actual amount.

Due to the low water vapor column amount in the USST-76 atmosphere the clear-sky estimates of the global average S_T, E_D, and E_U are irrealistic. The flux transmittance is over estimated by 33% and for example E_D is under estimated by about 31 W m^{-2}. The ERBE clear-sky OLR may also have a 6.5% positive bias. Although Eqs. (4) and (8) are satisfied, this discrepancy indicates that the USST-76 atmosphere does not represent a real radiative equilibrium temperature profile and should not be used as a single-column model for global energy budget studies.

It follows from Eq. (28) that $\pi B_0 = OLR(1-T_A)/2 = OLR(1+\hat{\tau}_C/2)$ and the characteristic optical depth will be equal to the total flux absorptance A. Those

optical depths where the source function is equal to E_U or E_D can also be easily derived: $\hat{\tau}_{E_U} = A - 2T_A/f$ and $\hat{\tau}_{E_D} = (2A/f) - T_A - 1$. Using large number of radiosonde observations, the global averages of πB_0, E_U, OLR, E_D, S_U, and their respective optical depths can be computed, and one can establish the dependence of optical depth on the z geometric altitude. In *Fig. 5*, on the right vertical axis, the 0, $\hat{\tau}_{E_U}$, $\hat{\tau}_C$, $\tilde{\tau}_A^C$, $\hat{\tau}_{E_D}$, and $\tilde{\tau}_A^E$ optical depths are also indicated. Note the close to linear relationship between the altitude and the optical depth. This relationship may be represented pretty well by the $\hat{\tau}(z) = \tilde{\tau}_A(1 - z/10)$ equation, where z is given in km. This linear function directly contradicts to the usual assumption of exponential decrease of $\tilde{\tau}(z)$ function, indicating the different nature of $\hat{\tau}(z)$. The optical depth computed from Eq. (21) is essentially the measure of the transfer of heat energy by non radiative processes and can be regarded as a kind of dynamical flux optical depth. Although $\hat{\tau}(0) = \tilde{\tau}_A$, the $\tilde{\tau}(z) = -\ln(T_A(z))$ is an exponential function and the $T_A(z)$ is a linear function. Let us mention that a linear $\hat{\tau}(z)$ function is consistent with the hydrostatic equation: $dp/d\hat{\tau} = g_a/\hat{k}$, where p is the atmospheric pressure, g_a is the gravity acceleration, and $\hat{k}$ is an effective absorption coefficient associated with $\hat{\tau}(z)$.

6. Error estimates

Eq. (28) was extensively validated against the results of large scale LBL simulations of the planetary flux optical depth and greenhouse effect, and selected satellite observations in *Miskolczi* and *Mlynczak* (2004). In *Fig. 7* we summarize the errors of the semi-infinite approximation using Eqs. (16) , (17), and (28). The comparison with Eq. (24) would be more complex, it involves real (or imposed) surface temperature discontinuity (through the term of S_G) and will be discussed elsewhere.

In the realistic range of the clear-sky $\tilde{\tau}_A$, Eq. (28) predicts 2–15% underestimates in the source function at the surface in Eq. (16), and about 25% overestimates in the surface upward radiation in Eq. (17). According to Eqs. (14) and (15), the response of the surface upward flux to a small optical depth perturbation, (CO_2 doubling, for example), is proportional to $\Delta\tilde{\tau}_A$. In the semi-transparent approximation $\Delta S_U(\tilde{\tau}_A) \approx \Delta\tilde{\tau}_A(1 - \exp(-\tilde{\tau}_A))$, which means that the semi-infinite approximation will seriously overestimate ΔS_U.

At a global average clear-sky optical depth the relative error is around 20%, but for smaller optical depth (polar areas) the error could well exceed 60%. Differences of such magnitude may warrant the re-evaluation of earlier greenhouse effect estimates. For the estimation of the greenhouse effect at some point all atmospheric radiative transfer model has to relate the flux

optical depth (or absorber amount) to the source function, therefore one should be aware of the errors they might introduce to their results when applying the semi-infinite approximation. The above sensitivity estimates assume a constant OLR, therefore, they should be regarded as initial responses for small optical depth perturbations. Considering the changes in the OLR as well, the correct theoretical prediction is $\Delta S_U / \Delta \tilde{\tau}_A = (A/4)OLR$.

For example, a hypothetical CO_2 doubling will increase the optical depth (of the global average profile) by 0.0241, and the related increase in the surface temperature will be 0.24 K. The related change in the OLR corresponds to –0.3 K cooling. This may be compared to the 0.3 K and –1.2 K observed temperature changes of the surface and lower stratosphere between 1979 and 2004 in *Karl et al.*, (2006).

From the extrapolation of the 'Keeling Curve' the estimated increase in the average CO_2 concentration during this time period is about 22% (*National Research Council of the National Academies*, 2004). Comparing the magnitude of the expected change in the surface temperature we conclude, that the observed increase in the CO_2 concentration must not be the primary reason of the global warming.

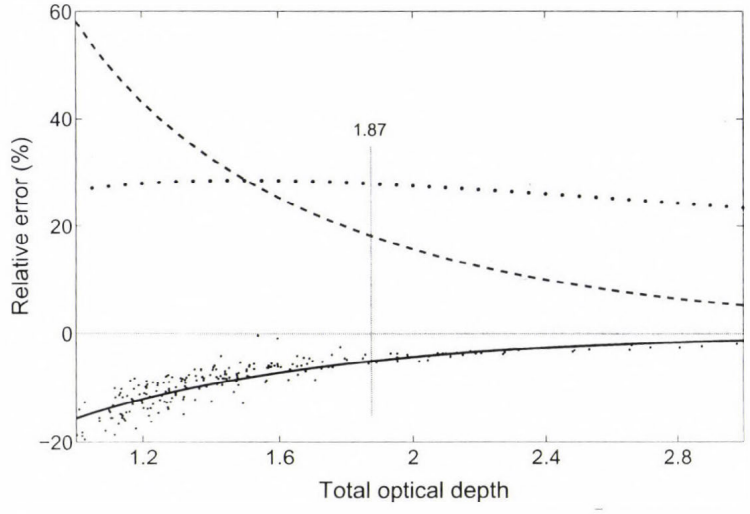

Fig. 7. The three relative error curves are: $f(\tilde{\tau}_A)\left[(1+\tilde{\tau}_A)/2 - 1/f(\tilde{\tau}_A)\right]$ (solid line), $f(\tilde{\tau}_A)\left[1+\tilde{\tau}_A/2 - 1/f(\tilde{\tau}_A)\right]$ (dotted line), and $1/(\exp(\tilde{\tau}_A)-1)$ (dashed line). These functions represent the relative differences using Eqs. (16) and (17) or Eq. (28) for the computation of $S_U(\tilde{\tau}_A)$ and $\Delta S_U(\tilde{\tau}_A)$, respectively. The vertical line is an estimate of the clear-sky global average $\tilde{\tau}_A$. The dots represent 228 LBL simulation results. The scatter of the dots is due to the fact that the temperature profiles were not in perfect radiative equilibrium.

7. Greenhouse parameters

The f and g functions may be used for the theoretical interpretation of some empirical greenhouse parameters: $G_1 = G_N = g$, and $G_2 = S_U / OLR = 1/f$. Here G_1 is Raval and Ramanathan's normalized greenhouse parameter, and G_2 is Stephens and Greenwald's greenhouse parameter (*Raval* and *Ramanathan*, 1989; *Stephens* and *Greenwald*, 1991). The sensitivity of the greenhouse function to optical depth perturbations is expressed by the derivative of g:

$$g_S = dg / d\tilde{\tau}_A = f^2 A / 2 . \tag{29}$$

The g_S function has a maximum at $\tilde{\tau}_A^S = 1.0465$, therefore, positive optical depth perturbations in the real atmosphere are coupled with reduced greenhouse effect sensitivity. Here we note, that the $g_S^\circ = 2T_A/5$ and $g_S^* = T_A/3$ sensitivities are decreasing monotonously with increasing $\tilde{\tau}_A$. It is also important that, due to the compensation effect of the combined linear and exponential optical depth terms, the f and g functions have negligible temperature dependence. There is, however, a slight non-linear dependence on the surface temperature introduced by the weighting of the monochromatic flux transmittances with the spectral S_U. Note, that the f and g functions can not be related easily to the absorber amounts, and, for example, a simple linear parameterization of them with the water vapor column amount could be difficult and inaccurate (*Stephens* and *Greenwald*, 1991; *Miskolczi* and *Mlynczak*, 2004).

The greenhouse parameters are dependent only on the flux optical depth, therefore it is difficult to imagine any water vapor feedback mechanism to operate on global scale. The global average $\tilde{\tau}_A^E$ is set by the global energy balance requirement of Eqs. (8) and (9).

It follows from Eqs. (8) and (28) that $3OLR/2 = OLR/f$ and $f = 2/3 = f^+$, giving an equilibrium optical depth of $\tilde{\tau}_A^+ = 1.841$. Using Eq. (9) and (28) the equilibrium optical depth becomes $\tilde{\tau}_A^\circ = 1.867$. The $\tilde{\tau}_A^E = 1.87$ is consistent with these theoretical expectations and the estimate of 1.79 in Section 3. The excess optical depth $\tilde{\tau}_A^E - \tilde{\tau}_A^+ = 0.029$ corresponds to about 1.5 W m^{-2} imbalance in S_U, which may temporarily be compensated for example by 1.0 W m^{-2} net heat flow from the planetary interior or by small decrease in the SW system albedo. In case of Eq. (9) the optical depth difference is even smaller, $\tilde{\tau}_A^E - \tilde{\tau}_A^\circ = 0.003$.

Since the world oceans are virtually unlimited sources and sinks of the atmospheric water vapor (optical depth), the system – depending on the time constant of the different energy reservoirs – has many ways to restore the equilibrium situation and maintain the steady state global climate. For example, in case the increased CO_2 is compensated by reduced H_2O, then the

general circulation has to re-adjust itself to maintain the meridional energy flow with less water vapor available. This could increase the global average rain rate and speed up the global water cycle resulting in a more dynamical climate, but still the energy balance equations do not allow the average surface temperature to rise. The general circulation can not change the global radiative balance although, changes in the meridional heat transfer may result in local or zonal warming or cooling which again leads to a more dynamical climate. Note that there are accumulating evidence of long term negative surface pressure trends all over the Southern Hemisphere (*Hines et al.*, 2000), which may be an indication of decreasing water vapor amount in the atmosphere.

The estimation of the absolute accuracy of the simulated global average $\tilde{\tau}_A^E$ is difficult. The numerical errors in the computations are negligible, and probably the largest single source of the error is related to the selection of the representative atmospheric profile set. To decide whether the indicated small optical depth differences are real, further global scale simulations are required.

In the view of the existence of the $\tilde{\tau}_A^+$ and $\tilde{\tau}_A^\circ$ critical optical depth, the runaway greenhouse theories have very little physical foundations. Greenhouse gases in any planetary atmosphere can only absorb the thermalized available SW radiation and the planetary heat flux. Keeping these flux terms constant, deviations from $\tilde{\tau}_A^+$ or $\tilde{\tau}_A^\circ$ will introduce imbalance in Eqs. (8) and (9), and sooner or later – due to the energy conservation principle – the global energy balance must be restored. On the long run the general energy balance requirement of Eq. (9) obviously overrules the IR radiative balance requirement of Eq. (28).

Based on Eq. (28) we may also give a simple interpretation of E_U: $E_U = S_U f - S_U T_A$. Since the total converted $F^0 + P^0$ to OLR is $S_U f$, and $S_U T_A$ is the transmitted part of the surface radiation, the $S_U f - S_U T_A$ difference is the contribution to the OLR from all other energy transfer processes which are not related to LW absorption: $E_U = F + K + P$. Substituting this last equation into the energy balance equation at the lower boundary, and using Eq. (3) we get: $E_D - A_A = 0$. This is the proof of the Kirchhoff law for the surface-atmosphere system. The validity of the Kirchhoff law requires the thermal equilibrium at the surface. Note, that in obtaining Eq. (28) the Kirchhoff law was not used (see Appendix B).

8. Zonal distributions

To explore the imbalance caused by optical depth perturbations, one has to use the differential form of Eq. (28):

$$\Delta f / f = \Delta OLR / OLR - \Delta S_U / S_U . \tag{30}$$

According to Eq. (30) the relative deviations from the equilibrium f, OLR, and S_U must be balanced. The validity of Eq. (30) is nicely demonstrated in *Fig. 8.*

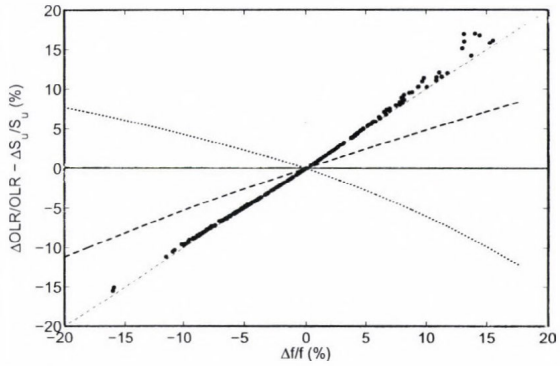

Fig. 8. Validation of the $\Delta f / f = \Delta OLR / OLR - \Delta S_U / S_U$ equation. Dots were computed from radiosonde observations and they represent the relative differences from the equilibrium f. The dashed and dotted lines are fitted to the $\Delta OLR / OLR$ and $\Delta S_U / S_U$ points, respectively.

The Δf can be related to the $\Delta \tilde{\tau}_A$ quantity through the $\Delta f = -\Delta \tilde{\tau}_A f^2 A / 2$ equation. The ΔOLR and ΔS_U quantities are defined by the next two equations: $\Delta OLR = -S_U \Delta \tilde{\tau}_A f^2 A / 4$ and $\Delta S_U = OLR \Delta \tilde{\tau}_A A / 4$. It can be shown that the $\Delta OLR / OLR + \Delta S_U / S_U = 0$, and $\Delta OLR = -f \Delta S_U$ equations also hold. In *Fig. 9* the dependence of ΔS_U on ΔOLR is presented. The open circles in this figure indicate small deviations from Eq. (30). At larger $|\Delta S_U|$ the true ΔOLR is slightly overestimated. *Figs. 8* and *9* show that the surface warming is coupled with reduced OLR, which is consistent with the concept of the stratospheric compensation.

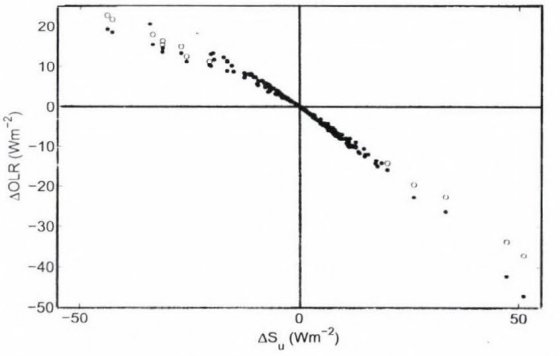

Fig. 9. The imbalance in S_U and OLR are marked with black dots. For the $|\Delta S_U| > 20$ W m^{-2} the open circles were computed from the $\Delta OLR = -f \Delta S_U$ equation.

Unfortunately, our static model can not deal with the dynamical factors represented by the variables K and F. The decomposition of E_U into its several components is beyond the scope of this study. Based on our large scale clear-sky simulations, in *Figs. 10, 11,* and *12* we present the meridional distributions of the zonal mean $\tilde{\tau}_A$, OLR, and S_U, and their deviations from Eqs. (8) and (28).

In *Fig. 10* the zonal average $\tilde{\tau}_A$ distributions are presented. At the equatorial regions up to about +/- 35 degree latitudes, the atmosphere contains more water vapor than the planetary balance requirement of $\tilde{\tau}_A^+$. This feature is the result of the combined effects of evaporation/precipitation processes and the transport of the latent and sensible heat by the general circulation. The reason of the differences between the actual and equilibrium zonal distributions is the clear-sky assumption. The global averages for both distributions are 1.87 representing about 2.61 prcm global average water vapor column amount.

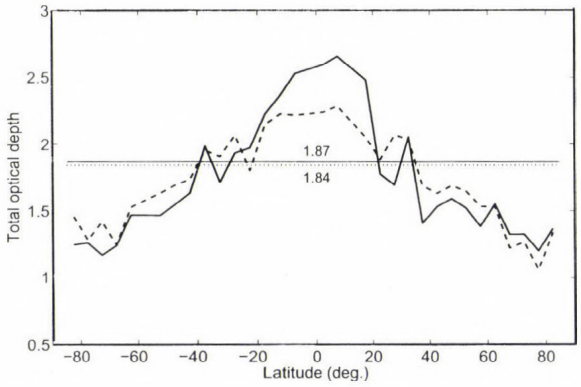

Fig. 10. Meridional distributions of the zonal mean clear sky $\tilde{\tau}_A$. Solid line is the actual $\tilde{\tau}_A$ computed from simulated flux transmittance. Dashed line is the required $\tilde{\tau}_A$ to satisfy the $2S_U / OLR - 1 = \tilde{\tau}_A + \exp(-\tilde{\tau}_A)$ equation. Thin solid horizontal line is the global average for both curves. Dotted line is the planetary equilibrium optical depth, $\tilde{\tau}_A^+$, obtained from Eqs. (6) and (26).

In *Fig. 11* the simulated OLR and the fS_U theoretical curve show good agreement at higher latitudes, indicating that for zonal means the IR radiative balance holds. At the equatorial regions the simulations significantly overestimate fS_U. The reason is the un-accounted cloud cover at low latitudes. The dotted line is the required OLR to completely balance the zonal mean S_U and can be regarded as the zonal mean clear-sky F^0.

In *Fig. 12* again, the effect of the cloud cover at low latitudes is the reason of the theoretical overestimation of S_U. At high latitudes Eq. (28) approximately holds. The dots were computed using the semi-infinite model, and

they show significant underestimation in the observed zonal mean S_U. According to *Figs. 11* and *12*, at higher latitudes the flux densities are almost balanced.

The quantitative analysis and the explanation of the imbalance at the equatorial regions requires further investigation involving large-scale simulations of cloudy atmospheres. It is also necessary to build a suitable theoretical broad band radiative transfer model for studying the different aspects of a complex multi-layer cloud cover. Using the new equations there is a hope that simple bulk formulation may be developed to deal with the planetary scale energetics of the cloud cover.

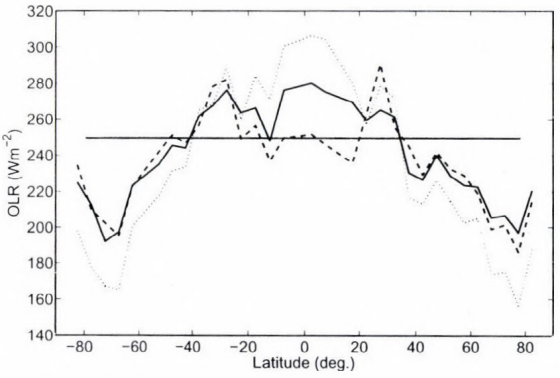

Fig. 11. Meridional distributions of the zonal mean OLR. Solid line is the actual clear-sky OLR computed from all sky radiosonde observations. Dashed line is the required OLR to satisfy the $OLR = f S_U$ equation. The horizontal line is the global average. Dotted line is the zonal mean equilibrium OLR computed as $2S_U/3$.

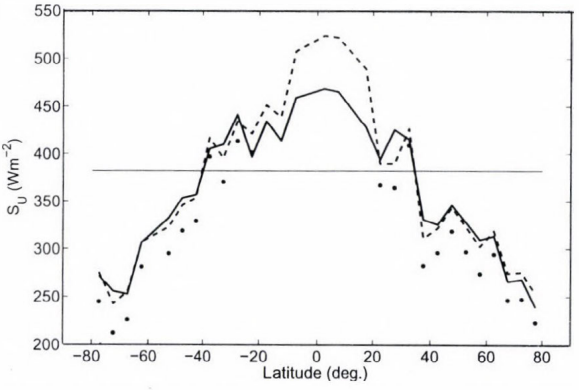

Fig. 12. Meridional distributions of the zonal mean surface upward flux densities. Thick solid line is the observed all sky S_U. Dashed line is the required S_U to satisfy the $S_U = OLR/f$ equation. Thin solid horizontal line is the global average. Dots represent the semi-infinite approximation of $S_U = OLR(1+\tilde{\tau}_A)/2$ for higher latitudes.

9. Planetary applications

The f, $f-T_A$, and g functions can be regarded as theoretical normalized radiative flux components representing OLR/S_U, E_U/S_U, and $(S_U-OLR)/S_U$ ratios, respectively. The f°, $f^\circ-T_A$, g°, and f^*, f^*-T_A, and g^* are similar functions representing Eqs. (9) and (10), respectively. The dependences of these functions and the g_S function on the optical depth are presented in *Fig. 13*. For reference, in this figure we also plotted the individual simulation results of E_U/S_U for the Earth and Mars, and the OLR/S_U only for the Mars. In the next sections we discuss some further characteristics of the broadband IR atmospheric radiative transfer of Earth and Mars.

At this time the Venusian atmosphere is not included in our study. The major problem with the Venusian atmosphere is the complete cloud cover and the lack of knowledge of the accurate surface SW and LW fluxes. The development of a comprehensive all-sky broadband radiative transfer model is in progress.

9.1 Earth

In *Fig. 13* the simulated global average normalized flux densities are very close to the theoretical curves, proving that the new equations reproduce the real atmospheric situations reasonably well. The horizontal scatter of the gray dots indicate the range of the optical depth that characteristic for the Earth's climate. Theoretically, the lower limit is set by the minimum water vapor amount and the CO_2 absorption. The upper limit is set by a theoretical limiting optical depth of $\tilde{\tau}_A^L = 2.97$, where the transfer and greenhouse functions becoming equal. This optical depth corresponds to about 6 prcm water vapor column amount, which is consistent with the observed maximum water vapor content of a warm and humid atmosphere.

The vertical scatter of the gray dots around the $f-T_A$ curve is the clear indication that locally the atmosphere is not in perfect radiative equilibrium and Eq. (28) is not perfectly satisfied. The obvious reason is the SW effect of the cloud cover and the more or less chaotic motion of the atmosphere. For the global averages Eqs. (8) and (28) represent strict radiative balance requirements. On regional or local scale this equation is not enforced by any physical law and we observe a kind of stochastic radiative equilibrium which is controlled by the local climate.

Over a wide range of optical depth around $\tilde{\tau}_A^U$, the $f-T_A$ curve is close to 0.5, which assures that E_U is approximately equal to $S_U/2$ independently of the gravitational constraint (virial theorem). This explains why Eqs. (9) and (25) can co-exist at the same $\tilde{\tau}_A^E$. The USST-76 atmosphere seems to follow the radiation scheme of Eqs. (8), $OLR/S_U \approx 2/3$. At the $\tilde{\tau}_A^{US}$ the global

radiative balance of the atmosphere is violated and the atmosphere can not be in radiative equilibrium either. The radiative balance and the radiative equilibrium can not co-exist at $\tilde{\tau}_A^{US}$. The radiative imbalance may be estimated from Eqs. (8) and (9) as $S_U(2/3-(1-2A/5)) \approx -10$ W m^{-2}. To retain the energy balance, the USST-76 atmosphere should lose about 10 W m^{-2} more IR radiation to space. The use of such atmospheres for global energy budget studies has very little merit.

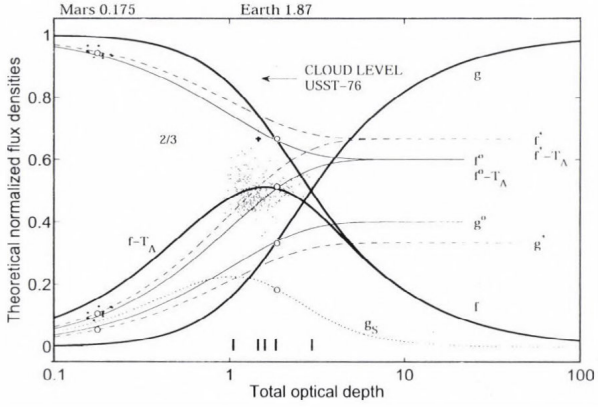

Fig. 13. Theoretical relative radiative flux ratio curves. Open circles are computed planetary averages from simulations. The individual simulation results of E_U / S_U are shown as gray dots for the Earth and black dots in the lower left corner for the Mars. The black dots in the upper left corner are the simulated OLR/S_U for Mars. The g_S curve is the theoretical greenhouse sensitivity function for the Earth. The five short vertical markers on the zero line at the positions of 1.05, 1.42, 1.59, 1.84, and 2.97 are (from left to right) the locations of $\tilde{\tau}_A^S$, $\tilde{\tau}_A^C \approx \tilde{\tau}_A^{US}$, $\tilde{\tau}_A^U$, $\tilde{\tau}_A^+ \approx \tilde{\tau}_A^\circ$, and $\tilde{\tau}_A^L$ optical depths, respectively.

This figure shows that the Earth has a controlled greenhouse effect with a stable global average $\tilde{\tau}_A^E = 1.87 \approx \tilde{\tau}^+ \approx \tilde{\tau}^\circ$, $g(\tilde{\tau}_A^E) = 0.33 \approx g^+ \approx g^\circ(\tilde{\tau}_A^E)$, and $g_S(\tilde{\tau}_A^E) \approx 0.185$. As long as the $F^0 + P^0$ flux term is constant and the system is in radiative balance with a global average radiative equilibrium source function profile, global warming looks impossible. Long term changes in the planetary radiative balance is governed by the $F^0 + P^0 = S_U(3/5 + 2T_A/5)$, $OLR = S_U f$ and $F^0 + P^0 = OLR$ equations. The system is locked to the $\tilde{\tau}_A^\circ$ optical depth because of the energy minimum principle prefers the radiative equilibrium configuration ($\tilde{\tau}_A < \tilde{\tau}_A^\circ$) but the energy conservation principle constrains the available thermal energy ($\tilde{\tau}_A > \tilde{\tau}_A^\circ$). The problem for example with the highly publicized simple 'bucket analogy' of greenhouse effect is the ignorance of the energy minimum principle (*Committee on Radiative Forcing Effects on Climate Change et al.*, 2005).

According to Eq. (9), a completely opaque cloudless atmosphere ($T_A \approx 0$) would accommodate a surface temperature of $\overline{t}_S = 288.3$ K, which is pretty close to the observed global average surface temperature. In this extent the LW effect of the cloud cover is equal to closing the IR atmospheric window and increasing the global average greenhouse effect by about 1.8 K, without changing the $\tilde{\tau}_A^E \approx \tilde{\tau}_A^\circ$ relation. The $\beta \approx 0.6$ cloud cover simultaneously assures the validity of the $OLR^A = \overline{S}_U(1 - 2\overline{A}/5) \approx 3\overline{S}_U/5$ radiation balance equation with $\overline{A} \approx 1$ and a global average $\overline{S}_U = 392$ W m^{-2}, and the radiative equilibrium clear-sky source function profile with $\tilde{\tau}_A^E = 1.87$. This could be the configuration, which maintains the most efficient cooling of the surface-atmosphere system.

9.2 Mars

We performed LBL simulations of the broadband radiative fluxes for eight Martian standard atmospheres. In *Fig. 14* the temperature and volume mixing ratio profiles are shown in the 0–60 km altitude range.

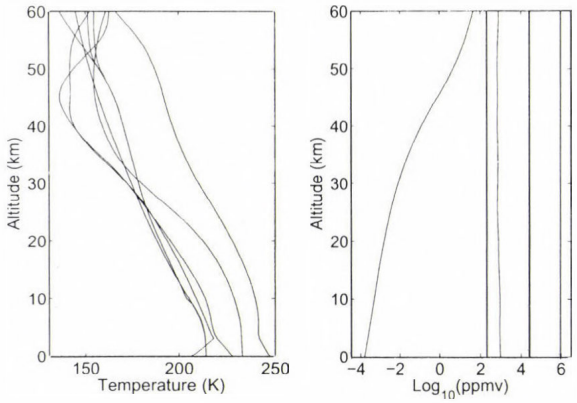

Fig. 14. Martian standard temperature and volume mixing ratio profiles. In the right plot the absorbers are (from left to right): O_3, H_2O, CO, N_2, and CO_2.

In *Fig. 15* dust-free clear-sky computed spectral *OLR* and S_U are presented for the coldest and warmest temperature profiles. The computations were performed in the 1–3490 cm^{-1} wavenumber range with 1 cm^{-1} spectral resolution. The single major absorption feature in these spectra is the 15 CO_2 band. The signatures of the 1042 cm^{-1} ozone band and several H_2O bands are present only in the upper (warmer) spectrum. Despite the almost pure CO_2 atmosphere, the clear Martian atmosphere is remarkably transparent. The

average flux transmittance is $T_A = 0.839$ (just about equal to the flux absorptance on the Earth), and the OLR is largely made up from S_T.

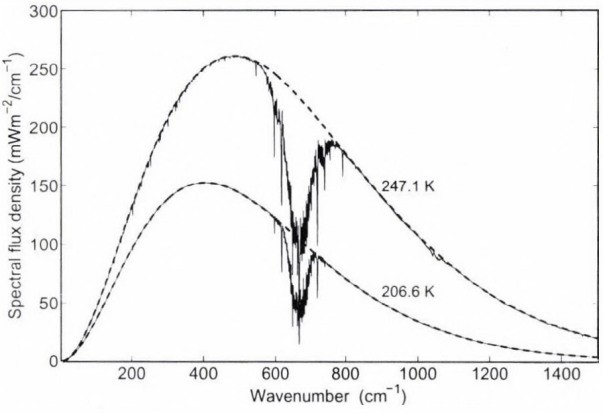

Fig. 15. LBL simulations of the spectral flux densities for a warm and a cold standard Martian atmospheric profile. The thin solid line is the spectral OLR and the thick dashed line is the blackbody function at the indicated surface temperatures.

In *Fig. 16* the relationships between S_U and S_T are shown for the Mars and Earth. In case of the Earth, S_T is almost independent of S_U, while in the Martian atmosphere the transmitted radiation depends linearly on the surface upward radiative flux. This fact is an indication that the broadband radiative transfer is fundamentally different on the two planets.

On Mars the optical depth has a strong direct dependence on the total mass of the atmosphere and consequently on surface pressure. The average flux optical depth is small, $\tilde{\tau}_A = 0.175 << \tilde{\tau}_A^+$. In *Fig. 13* the simulated OLR/S_U and E_U/S_U ratios systematically underestimate the theoretical f and $f - T_A$ functions. With the $P^0 \approx 0$ assumption, Mars does not satisfy the IR radiative equilibrium and the overall energy balance criteria at the surface.

For five model profiles the deviations from Eqs. (8) and (28) are presented in *Fig. 17.* The primary reason of the deviations related to the mechanism of the atmospheric heating by non IR radiative processes. On the Earth $K + F$ is large and sufficient to maintain the internal kinetic energy required by the surface pressure and the hydrostatic equilibrium ($E_U/S_U \approx 1/2$). The Martian atmosphere can not gain much energy through the K and F terms. The sublimation and condensation of CO_2 are mainly surface processes, no extended CO_2 cloud cover is observed. The visible and near IR absorption is also small, most of the SW flux is absorbed at the surface, consequently F is also small.

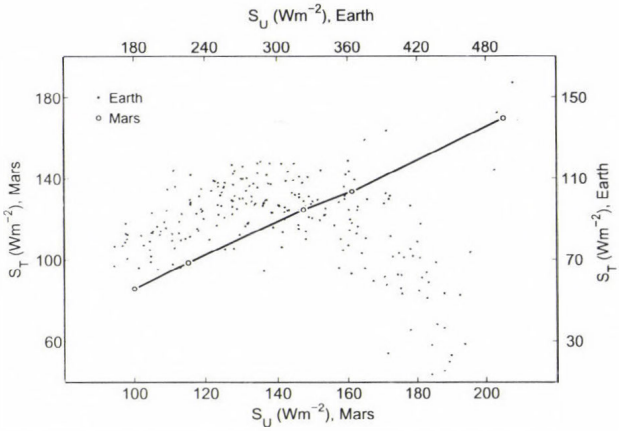

Fig. 16. Relationships between S_U and S_T. Data were obtained by LBL simulations using a set of Martian standard profiles and selected radiosonde observations from the TIGR radiosonde archive. In case of the Earth no significant linear correlation exists between S_U and S_T.

Simulation results show that the average E_U and S_U are 14.2 W m^{-2} and 134 W m^{-2}, respectively. The resulting $E_U / S_U \approx 0.1$ ratio is far too small to assure the hydrostatic equilibrium. In transparent atmospheres the $E_D/10$ term is usually small and may be ignored in Eq. (9). In case of Mars $E_D/10$ is about 1.5% of S_U, and apparently, the Martian atmosphere accommodates the radiative transfer scheme of Eq. (10).

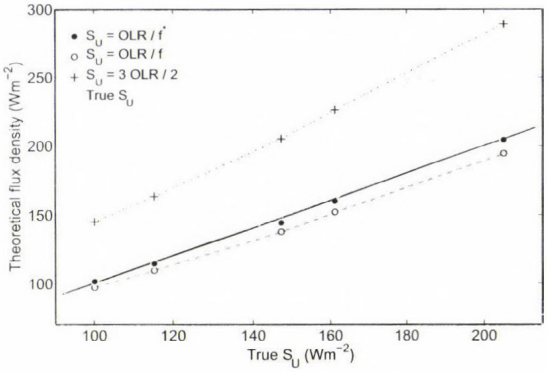

Fig. 17. Validation of the $f^* = 1 - A/3$ transfer function. The solid dots are the S_U fluxes computed with the new f^* transfer function. The 'true' S_U (solid line) were computed from the temperatures of the lowest levels of the standard Martian profiles via the Stefan-Boltzmann law. The 'o' and '+' symbols are the predictions of S_U using the f and the $S_U = 3OLR/2$ equations, respectively.

Using an average available absorbed SW radiation of 127 W m^{-2} Eq. (8) would require -56 W m^{-2} thermal energy to maintain the planetary energy balance. Simulation results show that S_T is 112.3 W m^{-2} and half of it could really restore the energy balance. Since the average E_U is small the $S_T/2$ flux term is the major contribution to the internal kinetic energy of the atmosphere. The wind blown atmospheric dust particles could have an important role in transferring this amount of thermal energy from the surface to the atmosphere. The f^* transfer function predicts both the true S_U in *Fig. 17* (solid dots) and the average relative OLR and E_U in *Fig. 13* (open circles) pretty well.

The linear dependence of $S_U f^*$ on $S_U T_A$ in *Fig. 16* explains why the band averaged spectral OLR/S_U ratio resolves the surface topography in the IR images in Chamberlain et al. (2006). The $f^* - T_A$ and g^* functions are also plotted in *Fig. 13*. The intersection of the f^* and f curves points to an optical depth of $\tilde{\tau}_A^* = 1.451$ where the atmosphere would be in radiative equilibrium with a linear average source function profile. At this $\tilde{\tau}_A^*$ the $E_D/10$ term in Eq. (9) becoming large, the approximation of Eq. (10) will not hold, and consequently the radiative balance can not exist. The error of Eq. (10) increases with increasing optical depth.

Regarding the range of the variability of the optical depth (or surface pressure) this situation can not occur in the clear Martian atmosphere. In the radiation scheme of Eq. (10) the runaway greenhouse effect is impossible, S_U will tend to $3OLR/2$ with increasing optical depth.

A further interesting consequence of Eq. (10) is the $2E_D - 3E_U = 0$ relationship. For the deeper understanding of these types of balance equations, in *Figs. 18* and *19* the spectral flux density differences are plotted around the central region of the 15 μm CO_2 absorption band.

In *Fig. 18* the band averaged differences of both the thick and thin solid curves are represented with a single dotted line at the zero position. We see that the spectral deviations of both the $S_U - OLR/f^*$ and $3OLR/2 - (S_U + S_T/2)$ spectral differences are almost perfectly compensated, assuring the validity of the respective balance equations. In *Fig. 19* similar explanation holds for the validity of the $2E_D - 3E_U = 0$ relationship. In this case the integral of the spectral $2E_D - 3E_U$ over the 1–3490 cm^{-1} range is 0.04 W m^{-2} only.

The average normalized greenhouse factor G_N is 0.0522, which is consistent with the $A/3 = 0.0536$ theoretical value. The $G = 7.1$ W m^{-2} greenhouse factor gives 3 K greenhouse enhancement to the planetary average surface temperature. The greenhouse sensitivity is $df^*/d\tilde{\tau}_A = T_A/3 = 0.23$ per unit optical depth and always decreasing with increasing $\tilde{\tau}_A$.

We may conclude, that Eq. (10) adequately describes the broadband radiative fluxes in the Martian atmosphere, but for planets with significantly larger optical depths Eq. (9) must be used.

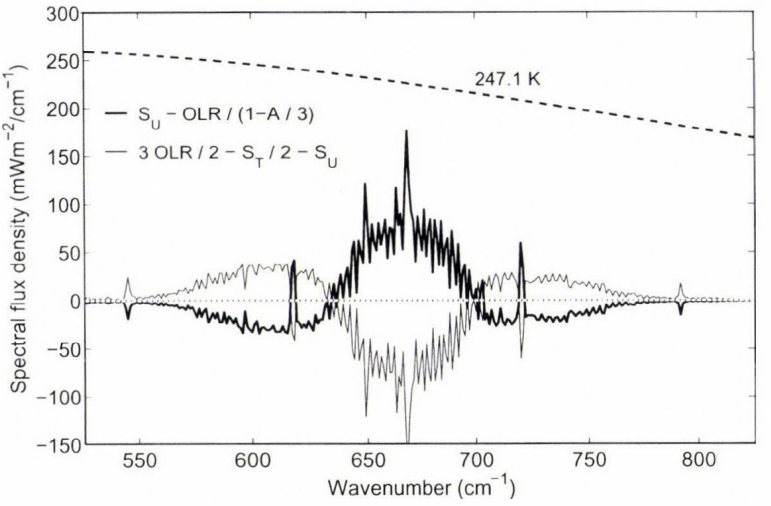

Fig. 18. Spectral flux differences in the 15 μm CO_2 band. The dotted line represents the averaged differences over the 1–3490 cm^{-1} spectral range for both curves. The dashed line is the spectral blackbody radiation at the indicated surface temperature. The spectral differences are compensated over a relatively narrow wavenumber interval around the band center.

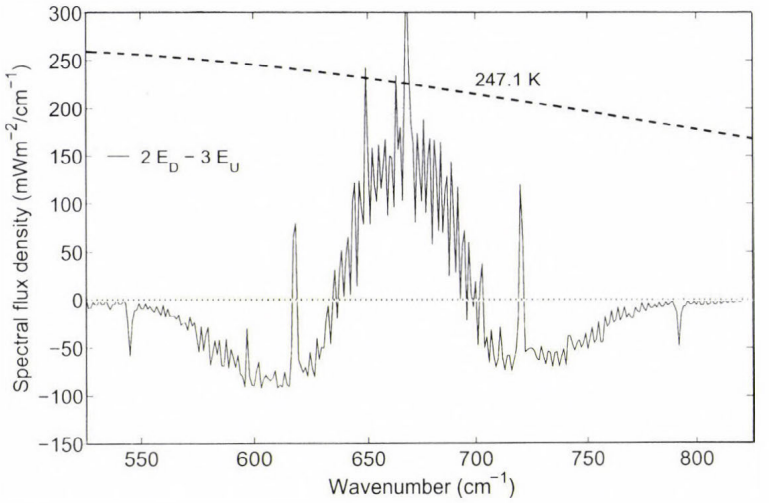

Fig. 19. Spectral differences in the $2E_D$ and $3E_U$ flux densities. The dotted line represents the averaged differences over the 1–3490 cm^{-1} spectral range. The dashed line is the spectral blackbody function at the indicated surface temperature. The spectral differences are largely compensated over the extent of the 15 μm CO_2 band.

10. Conclusions

The purpose of this study was to develop relevant theoretical equations for greenhouse studies in bounded semi-transparent planetary atmospheres in radiative equilibrium. In our terms the local radiative equilibrium is a unique instantaneous state of the atmosphere where the upward atmospheric radiation is balanced by the short wave atmospheric absorption and the net exchange of thermal fluxes of non-radiative origin at the boundary. In general, the thermal structure of the atmosphere assures that the absorbed surface upward radiation is equal to the downward atmospheric radiation. It seems that the Earth's atmosphere maintains the balance between the absorbed short wave and emitted long wave radiation by keeping the total flux optical depth close to the theoretical equilibrium values.

On local scale the regulatory role of the water vapor is apparent. On global scale, however, there can not be any direct water vapor feedback mechanism, working against the total energy balance requirement of the system. Runaway greenhouse theories contradict to the energy balance equations and therefore, can not work. We pointed to the importance of a characteristic altitude of about 2 km, where the cloud cover may control the SW input of the system without changing the global average OLR. To explain the observed increase in the global average surface temperature probably more attention should be paid to the changes in the net contribution from the F^0 and P^0 flux terms and changes in the global average water vapor content and cloud cover. Instead of the USST-76 atmosphere, further global energy budget studies should use appropriate zonal and global average atmospheres which satisfy the global radiative balance requirement and comply with the physics of the global greenhouse effect.

Eqs. (21) and its derivatives are theoretically sound and mathematically correct relationships between the fluxes, greenhouse parameters, and the flux optical depths, and they are good enough to give quantitative estimates with reasonable accuracy. One of the most important results is the derived $S_U = OLR / f$ functional relationship which replaces the mathematically incorrect $S_A = OLR(1+\tilde{\tau}_A)/2$ and $S_G = OLR(2+\tilde{\tau}_A)/2$ equations (classic Eddington solutions), and also resolves the surface temperature discontinuity problem. In radiative equilibrium the thermal equilibrium at the surface is the consequence of the energy minimum principle and it is an explicit requirement of the new equations.

We showed that, by applying the semi-infinite atmospheric model for clear or optically thin atmospheres, large errors may be introduced into the equilibrium surface temperatures. An other important consequence of the new equations is the significantly reduced greenhouse effect sensitivity to optical

depth perturbations. Considering the magnitude of the observed global average surface temperature rise and the consequences of the new greenhouse equations, the increased atmospheric greenhouse gas concentrations must not be the reason of global warming. The greenhouse effect is tied to the energy conservation principle through the $S_U + S_T/2 - E_D/10 = 3(F^0 + P^0)/2 = 3S_U f/2$ equations and can not be changed without increasing the energy input to the system.

Applying the virial theorem new radiative balance equations were derived. We showed that the clear Martian model atmospheres are not in radiative equilibrium. The new transfer and greenhouse functions adequately describe the planetary greenhouse effect on the Mars and Earth. The formulation of the new theory for the completely cloudy Venusian atmosphere is in progress.

The basic limitations of our formulas are related to the Eddington, and LTE approximations, and – regarding the practical applications – the assumption of the radiative balance and radiative equilibrium. The simplicity and compactness of the formulas make the flux calculations easy and fast and make them good candidates for greenhouse effect parameterizations in sophisticated climate models. Reasonable global change assessment using GCMs is only possible by observing the basic physical principles governing the planetary greenhouse effect. Regarding the economical impact of the global warming the identification of the real causes of the warming should have the highest priority of the climate research. We believe that the fundamental physics of the greenhouse effect in semi-transparent planetary atmospheres is clearly reflected in the new equations and once the new greenhouse theory may even appear in textbooks on the atmospheric radiative transfer.

Acknowledgements—It is my privilege to publish this paper in the Időjárás. I wish to thank for the support and encouragement obtained from *G. Major, Sz. Barcza, Z. Tóth, M. Zágoni, L. Bozó, K. Sifrin, K. Rutledge, K. Vinnikov*, and *S. Gupta*. I am also very grateful to *M. Antal* for her help with the final editing of the manuscript.

Appendix A: Flux optical depth

The usual definition of the gray-body optical depth is the $d\bar{\tau} = \bar{k}\,du$ equation, where $\bar{k}$ is a properly averaged absorption coefficient over the wavenumber domain, and u is the total amount of a particular absorber along the optical path. Regarding an S_0 LW radiative flux passing through a homogeneous absorbing layer, it is expected that the transmitted part of S_0 satisfies the next equations: $S(\bar{\tau}) = S_0 \exp(-\bar{\tau}) = S_0 \exp(-\bar{k}u)$ and $S(0) = S_0$. In general, for a mixture of different kind of absorbers having complex overlapping rotational-vibrational band structures no such weighted average absorption coefficient (and effective absorber amount) can be computed a-priori. However, for an

inhomogeneous layered atmosphere the exact flux optical depth may be obtained by using the LBL method. The first step is to compute the directional mean transmittances over a suitable short wavenumber interval:

$$\bar{T}_A(\Delta\nu,\mu)=\frac{1}{\Delta\nu}\int_{\Delta\nu}\exp\left[-\sum_{l=1}^{L}\sum_{i=1}^{N}\left[c^{i,l}+k_\nu^{i,l}\right]\frac{u^{i,l}}{\mu^l}\right]d\nu\,, \tag{A1}$$

where $\mu^l=\cos(\theta^l)$ and θ^l is the local zenith angle, $c^{i,l}$ and $k_\nu^{i,l}$ are the contributions to the total monochromatic absorption coefficient from the continuum type absorptions and all absorption lines relevant to the *i*th absorber and *l*th layer, respectively. $N=11$ is the total number of major absorbing molecular species and $L=150$ is the total number of the homogeneous atmospheric layers. In HARTCODE the wavenumber integration is performed numerically by 5th order Gaussian quadrature over a wavenumber mesh structure of variable length. At least $\Delta\nu=1\,\mathrm{cm}^{-1}$ spectral resolution is required for the accurate Planck weighting. The hemispheric spectral flux transmittance is obtained by integrating Eq. (A1) with respect the solid angle:

$$\tilde{T}_A(\Delta\nu)=\int_{2\pi}\bar{T}_A(\Delta\nu,\mu)d\omega\,. \tag{A2}$$

In the computation of the integral in Eq. (A2) nine streams (zenith angles) were used and the cylindrical symmetry of the radiation field was also assumed. The Planck-weighted hemispheric mean transmittances were computed from $\tilde{T}_A(\Delta\nu)$ by the following sum:

$$T_A=\frac{1}{\sigma t_A^4}\sum_{j=1}^{M}\pi B(\Delta\nu_j,t_A)\tilde{T}_A(\Delta\nu_j)\,, \tag{A3}$$

where $M=3490$ is the total number of spectral intervals, t_A is the surface temperature, and $B(\Delta\nu_j,t_A)$ is the averaged Planck function over $\Delta\nu_j$. Since the sum in Eq. (A3) is obviously the total transmitted radiative flux from the ground, the exact flux optical depth may be expressed as:

$$\tilde{\tau}_A=-\ln(T_A)\,. \tag{A4}$$

The dependence of $\tilde{\tau}_A$ on the individual total absorber amounts still can not be computed directly, but using a pre-computed database the construction of a $\tilde{\tau}_A(u^1,u^2,\ldots,u^N)$ function is a matter of a multi-dimensional parameterization. Here $u^1,\ldots,u^N$ represent the column amounts of the different greenhouse

gases. Such parameterization may also contain the effective temperature and pressure of the absorbers.

Appendix B: Source function profile in bounded atmosphere

We have seen that in a semi-transparent atmosphere the surface upward radiation is $B_G = \varepsilon_G \sigma t_G^4 / \pi$, and the upper boundary condition at the top of the atmosphere is the zero downward IR radiance. The upward and downward hemispheric mean radiance at the upper boundary using the general classic solution of the plane-parallel radiative transfer equation and the isotropy approximation are:

$$\overline{I}^{+}(0) = B_G e^{-\frac{3}{2}\overline{\tau}_A} + \frac{3}{2}\int_0^{\overline{\tau}_A} B(\overline{\tau}') e^{-\frac{3}{2}\overline{\tau}'} d\overline{\tau}', \tag{B1}$$

and

$$\overline{I}^{-}(0) = 0. \tag{B2}$$

Putting Eq. (B1) and Eq. (B2) into the $H(\overline{\tau}) = \pi(\overline{I}^{+} - \overline{I}^{-})$ equation, and substituting the source function with $B(\overline{\tau}) = 3H(\overline{\tau})/(4\pi) + B_0$ in the upward hemispheric mean radiance we get:

$$\frac{H}{\pi} = B_G e^{-\frac{3}{2}\overline{\tau}_A} + \frac{3}{2}\int_0^{\overline{\tau}_A} \frac{3H}{4\pi}\overline{\tau}' e^{-\frac{3}{2}\overline{\tau}'} d\overline{\tau}' + \frac{3}{2}\int_0^{\overline{\tau}_A} B_0 e^{-\frac{3}{2}\overline{\tau}'} d\overline{\tau}'. \tag{B3}$$

The two definite integrals in the second and third terms of the right hand side of Eq. (B3) must be evaluated:

$$\frac{3}{2}\int_0^{\overline{\tau}_A} \frac{3H}{4\pi}\overline{\tau}' e^{-\frac{3}{2}\overline{\tau}'} d\overline{\tau}' = -\frac{H}{4\pi}(2e^{-\frac{3}{2}\overline{\tau}_A} - 2 + 3\overline{\tau}_A e^{-\frac{3}{2}\overline{\tau}_A}), \tag{B4}$$

$$\frac{3}{2}\int_0^{\overline{\tau}_A} B_0 e^{-\frac{3}{2}\overline{\tau}'} d\overline{\tau}' = B_0(1 - e^{-\frac{3}{2}\overline{\tau}_A}). \tag{B5}$$

After putting back Eqs. (B4) and (B5) into Eq. (B3) we get:

$$\frac{H}{\pi} = B_G e^{-\frac{3}{2}\overline{\tau}_A} + \frac{H}{4\pi}(2e^{-\frac{3}{2}\overline{\tau}_A} - 2 + 3\overline{\tau}_A e^{-\frac{3}{2}\overline{\tau}_A}) + B_0(1 - e^{-\frac{3}{2}\overline{\tau}_A}). \tag{B6}$$

Rearranging Eq. (B6) and using the $\tilde{\tau}_A = (3/2)\bar{\tau}_A$ notation for the total flux optical depth, πB_0 can be expressed as:

$$\pi B_0 = \frac{\frac{H}{2}\left[1 + \tilde{\tau}_A e^{-\tilde{\tau}_A} + e^{-\tilde{\tau}_A}\right] - \pi B_G e^{-\tilde{\tau}_A}}{1 - e^{-\tilde{\tau}_A}}. \tag{B7}$$

This B_0 in the $B(\bar{\tau}) = 3H(\bar{\tau})/(4\pi) + B_0$ equation will give the general form of the source function profile:

$$\pi B(\tilde{\tau}) = \frac{\frac{H}{2}\left[1 + \tilde{\tau} + (\tilde{\tau}_A - \tilde{\tau} + 1)e^{-\tilde{\tau}_A}\right] - \pi B_G e^{-\tilde{\tau}_A}}{1 - e^{-\tilde{\tau}_A}}. \tag{B8}$$

Applying the $T_A = \exp(-\tilde{\tau}_A)$, $A = 1 - T_A$, and $f = 2/(1 + \tilde{\tau}_A + Tr_A)$ notations, Eq. (B8) will become identical with Eq. (21). The semi-infinite solution may be obtained exactly in the same way, but substituting $\tilde{\tau}_A$ with infinity in Eq. (B1), or simply by making these substitutions in Eq. (B8).

The most efficient cooling of the clear atmosphere requires a total optical depth that maximizes B_0. The derivative of Eq. (B7) with respect $\tilde{\tau}_A$ may be expressed as:

$$\pi \frac{dB_0(\tilde{\tau}_A)}{d\tilde{\tau}_A} = \frac{d}{d\tilde{\tau}_A}\left[\frac{\frac{OLR}{2}\left[1 + \tilde{\tau}_A + e^{\tilde{\tau}_A}\right] - \pi B_G}{e^{\tilde{\tau}_A} - 1}\right] \tag{B9}$$

From Eq. (B9) follows that:

$$\frac{\pi B_G e^{\tilde{\tau}_A} - \frac{OLR}{2}\left[1 + e^{\tilde{\tau}_A} + \tilde{\tau}_A e^{\tilde{\tau}_A}\right]}{\left(e^{\tilde{\tau}_A} - 1\right)^2} = 0. \tag{B10}$$

From Eq. (B10), assuming $\tilde{\tau}_A > 0$ we get:

$$\pi B_G = OLR\frac{1 + \tilde{\tau}_A + e^{-\tilde{\tau}_A}}{2} = \frac{OLR}{f}. \tag{B11}$$

Combining this equation with Eq. (28) we obtain the $\pi B_G = S_U$ equivalence requiring the thermal equilibrium at the ground surface. Note, that at real ground or sea surfaces the $\varepsilon_G \neq 1$ condition will result in the $S_G \neq S_A$ inequality, which is also apparent in *Fig. 2*.

References

Chamberlain, S.A., Bailey, J.A., and *Crisp, D.*, 2006: Mapping Martian atmospheric pressure with ground-based near infrared spectroscopy. *Publications of the Astronomical Society of Australia, 23*, 119-124.

Collins, G.W. II., 2003: *The Fundamentals of Stellar Astrophysics. Part II. Stellar Atmospheres.* WEB edition, 306 pp.

Committee on Radiative Forcing Effects on Climate Change, Climate Research Committee, and *National Research Council*, 2005: *Radiative Forcing of Climate Change: Expanding the Concept and Addressing Uncertainities*. The National Academies Press, USA.

Eddington, A.S., 1916: On the radiative equilibrium of the stars. *Monthly Notices of the Royal Astronomical Society*, LXXVII. I, 16-35.

ERBE, 2004: *ERBE Monthly Scanner Data Product*. NASA LRC, Langley DAAC User and Data Services. userserv@eosdis.larc.nasa.gov.

Goody, R.M. and *Yung, Y.L.*, 1989: *Atmospheric Radiation. Theoretical Basis*. University Press, Inc., Oxford, 392 pp.

Hines, K.M., Bromwich, D.H., and *Marshall, G.J.*, 2000: Artificial surface pressure trends in the NCEP-NCAR reanalysis over the southern ocean and Antarctica. *J. Climate 13*, 3490-3952.

Inamdar, A.K. and *Ramanathan, V.*, 1997: On monitoring the atmospheric greenhouse effect from space. *Tellus 49B*, 216-230.

Karl, T.R., Hassol, J.S., Miller, D.C., and *Murray, W.L.*, 2006: *Temperature Trends in the Lower Atmosphere*. U.S. Climate Change Science Program, Synthesis and Assessment Product 1.1, http://www.climatescience.gov.

Kiehl, J.T. and *Trenberth, K.E.*, 1997: Earth's annual global mean energy budget. *B. Am. Meteorol. Soc. 78*, 197-208.

Lorenz, R.D. and *McKay, C.P.*, 2003: A simple expression for vertical convective fluxes in planetary atmospheres. *Icarus*, 165, 407-413.

McKay, C.P., Lorenz, R.D., and *Lunine, J.I.*, 1999: Analytic solutions for the antigreenhouse effect: Titan and the early Earth. *Icarus*, 137, 56-61.

Milne, A.E., 1922: Radiative equilibrium: the insolation of an atmosphere. *Monthly Notices of the Royal Astronomical Society*, XXIV, 872-896.

Miskolczi, F.M. and *Mlynczak, M.G.*, 2004: The greenhouse effect and the spectral decomposition of the clear-sky terrestrial radiation. *Időjárás 108*, 209-251.

Miskolczi, F.M., Bonzagni, M., and *Guzzi, R.*, 1990: High-resolution atmospheric radiance-transmittance code (HARTCODE). In *Meteorology and Environmental Sciences: Proc. of the Course on Physical Climatology and Meteorology for Environmental Application*. World Scientific Publishing Co. Inc., Singapore.

National Research Council of the National Academies, 2004: *Climate Data Records from Environmental Satellites*. The National Academies Press, Washington DC.

Peixoto, J.P. and *Oort, A.H.*, 1992: *Physics of Climate*. American Institute of Physics, New York.

Raval, A. and *Ramanathan, V.*, 1989: Observational determination of the greenhouse effect. *Nature, 342*, 758-761.

Sagan, C., 1969: On the structure of the Venusian atmosphere. *Icarus*, 10, 274-289.

Stephens, G.L. and *Greenwald, T.J.*, 1991: The Earth's radiation budget and its relation to atmospheric hydrology 1. observations of the clear-sky greenhouse effect. *J. Geophys. Res. 96*, 15311-15324.

Stephens, G.L., Slingo, A., and *Webb, M.*, 1993: On measuring the greenhouse effect of Earth. *NATO ASI Series, Vol. 19*, 395-417.

Weaver, C.P. and *Ramanathan, V.*, 1995: Deductions from a simple climate model: factors governing surface temperature and thermal structure. *J. Geophys. Res. 100*, 11585-11591.

IDŐJÁRÁS

Quarterly Journal of the Hungarian Meteorological Service
Vol. 111, No. 1, January–March 2007, pp. 41–63

The Constitution Day storm in Budapest: Case study of the August 20, 2006 severe storm

Ákos Horváth[1*], István Geresdi[2], Péter Németh[3] and Ferenc Dombai[3]

[1]*Hungarian Meteorological Service, Storm Warning Observatory, Vitorlás u. 17, H-8600 Siófok, Hungary; E-mail: horvath.a@met.hu*

[2]*University of Pécs, Institute of Environmental Sciences, Ifjúság u. 6, H-7624 Pécs, Hungary; E-mail: geresdi@gamma.ttk.pte.hu*

[3]*Hungarian Meteorological Service, P.O. Box 39, H-1675 Budapest, Hungary; E-mails: nemeth.p@met.hu; dombai.f@met.hu*

(Manuscript received in final form March 5, 2007)

Abstract—In the evening of August 20, 2006 severe thunderstorms hit Budapest. The storm struck the downtown at the same time when the Constitution Day firework just started, killed five people and wounded hundreds of spectators crowded on the embankments of the river Danube. In this paper weather conditions from synoptic scale to storm scale are investigated to find the special circumstances, which led to formation of the devastating storm. Investigations show that a wave on a cold front, the mid level cold advection, the drift of jet stream above the warm sector, and an intense wet conveyor belt resulted in intense instability. Furthermore, the wind shear and the low level convergence also contributed to the formation of the fast moving squall line. Detailed Doppler-radar analysis proved that the thunderstorm, which crossed the downtown of Budapest, was a supercell. Comparison of the radar reflectivity and the lightning data of the investigated case with that of other severe storm cases shows that the Constitution Day storm was not an extreme event. The unique feature of this case was the extreme high speed of cell motions. High resolution numerical model (MM5) was applied to understand the dynamical structure and predictability of the storm. Model results show the importance of the layer on 3 km above ground level with high value of equivalent potential temperature and the active role of the cold front in the formation of the squall line. The model was able to simulate the structure and motion of the supercell proving the numerical predictability of this type of severe convective storms.

Key-words: squall line, supercell, MM5, severe convective storm, Doppler-radar

Corresponding author

1. Introduction

Late afternoon on August 20, 2006, a squall line coming from the north-west direction reached the western border of Hungary. Surface and radar observations showed, that thunderstorm cells moved fast and some of them were extremely intensive. The north part of the squall line arrived in Budapest at 19:00 UTC, when the traditional Constitution Day's firework had just started. In the centre of Budapest, more than half million people crowded on the embankments and bridges of the river, and numerous spectators watched the event from boots drifting on the Danube, too. The thunderstorm produced wind gusts reached 32.3 m/s in the centre of downtown (measured on the top of the building of the Hungarian Meteorological Service), and 34.1 m/s in the southern part of the downtown (measured on the top of the building of the University of Science). Broken trees and fragments from roof of houses hit into crowds causing injuries and panic. Five people were killed and hundreds were injured due to the extreme weather. The strong wind caused a loss of about 5 million USD in buildings and cars.

Severe thunderstorms and associated phenomena like stormy wind gusts, hailstorms, heavy rainfalls, sometimes tornadoes often occur in Hungary, especially in summer. The facts presented in this paper suggest that this storm was a supercell thunderstorm, one of the types of severe convective phenomena which are observed from time to time in Hungary (*Horváth* and *Geresdi*, 2003). Structure and development of severe convective phenomena have been investigated since the beginning of the 1950's. Among others, pioneering work of Fujita described the phenomenology of squall lines (*Fujita*, 1955), and the origin of thunderstorm pressure-heights (*Fujita et al.*, 1959). Meteorological satellites and radars have become the main tools for investigation and operative forecast of severe convection (*Reyonolds et al.*, 1979). These remote sensing equipments and the surface meso-networking observations allowed to develop comprehensive theories of the mesoscale convective system (MCS) such as long-lived squall lines (*Rotunno et al.*, 1988; *Houze et al.*, 1989). The most devastating mesoscale phenomena are the supercells which are mostly associated with MCS. The presently accepted theory about the dynamics and necessary conditions of supercell formation was published by *Klemp* (1987). Most of the MCSs and supercells form in the unstable region of cyclones and frontal systems. Prefrontal conditions – large convective available potential energy, horizontal and vertical wind shears (*Davies-Jones et al.*, 2001) – can produce favorable environment for the supercell formation. The convergence and vertical circulation of frontal system (*Hoskins*, 1972) also promote the MCS formation, especially if the MCS is connected with the circulation of the jet stream (*Shapiro*, 1982).

The first numerical experiments about the simulation of convective storms used twodimensional models in the 1960's (*Lilly*, 1962). The large computer capacity necessary for the three-dimensional simulation of thunderstorms (e.g., *Klemp*, 1978) was available by the late 70's. Supercells and squall lines are very complex atmospheric phenomena, so they can be simulated only with state-of art numerical models which involves non-hydrostatic version of equation of motion, detailed description of short and long wave radiation, processes occuring in the boundary layer, and formation of precipitation and cloud elements (*Wilhelmson*, 2001).

Early investigations of severe thunderstorms in Hungary were motivated by improving the efficiency of the storm warning at Lake Balaton (*Götz*, 1966; *Böjti et al.*, 1964; *Götz*, 1968). The hail suppressing system operated in the 1980's required the investigation of microphysical processes occuring in thunderstorms (*Zoltán* and *Geresdi*, 1984). Dynamical conditions of the formation of squall lines in the Carpathian Basin were investigated by *Horváth* and *Práger* (1985). *Bartha* (1987) worked out an empirical method to predict maximum wind gusts of thunderstorm cells. *Bodolainé* and *Tänczer* (2003) investigated flash flood causing mesoscale convective complexes in the Carpathian Basin. The nowcasting system of the Hungarian Meteorological Service gave a new tool for the ultrashort term forecast of severe weather (*Geresdi* and *Horváth*, 2000; *Horváth* and *Geresdi*, 2003; *Geresdi et al.*, 2004). Appearances of supercells and formation of tornadoes in Hungary was described first time by *Horváth* (1997). Due to the increased authenticity of radar in the weather radar network of Hungarian Meteorological Service (HMS) by the end of the 90's, more supercell cases were recognized (*Horváth*, 1997; *Horváth* and *Geresdi*, 2003). Not only the observation background has been improved, but a new tool for the numerical simulation of supercells and tornadoes became available by using limited area non-hydrostatic model MM5 (*Horváth et al.*, 2006).

In the first section of the paper the synoptic scale conditions of formation and development of the Budapest storm are shown by using ECMWF analysis and forecast. In the second section the development, movement, and other characteristics of the storm cells are analyzed by using radar data. In the third section results of MM5 model with high resolution are discussed. The general and special features, furthermore, the predictability of the Budapest storm are given in the conclusion.

2. Synoptic scale weather conditions

On August 20, 2006 a long and thermally sharp cold front crossed Central and Southern Europe moving to the east. On the 850 hPa pressure level the temperature difference between the warm sector and the postfrontal region was

10–12 °C. In the southern part of the long frontal system, between 00:00 and 12:00 UTC, a frontal wave developed. This wave – behaving like a temporary warm front – expanded to the Alps by 15:00 UTC (*Fig. 1*). The dotted line in *Fig. 1* represents the leading edge of a weak high level cold airmass, which moved above the warm sector. Signs of this high level cold advection can be seen in the figure of 500 hPa temperature and wind fields (*Fig. 2*). The high level cold air could move there, because the low level wave of the long cold frontal system did not affect upper streams, and they continued their drifting toward the east. In the cross section of potential vorticity field a positive local maximum can also be associated with the mid tropospheric cold advection (*Fig. 3*). The second important feature of the weather pattern is the extremely intense wet conveyor belt at the 700 hPa level (*Fig. 4*). In the layer of the wet conveyor belt the maximum values of relative humidity coincided with the significant wind maximum, which could be considered as the low level jet stream. The third characteristic is the upper level jet stream at the 300 hPa level (*Fig. 5*). The upper level strong wind results in vertical wind shear necessary for the formation of severe convective storm (*Holton*, 2004).

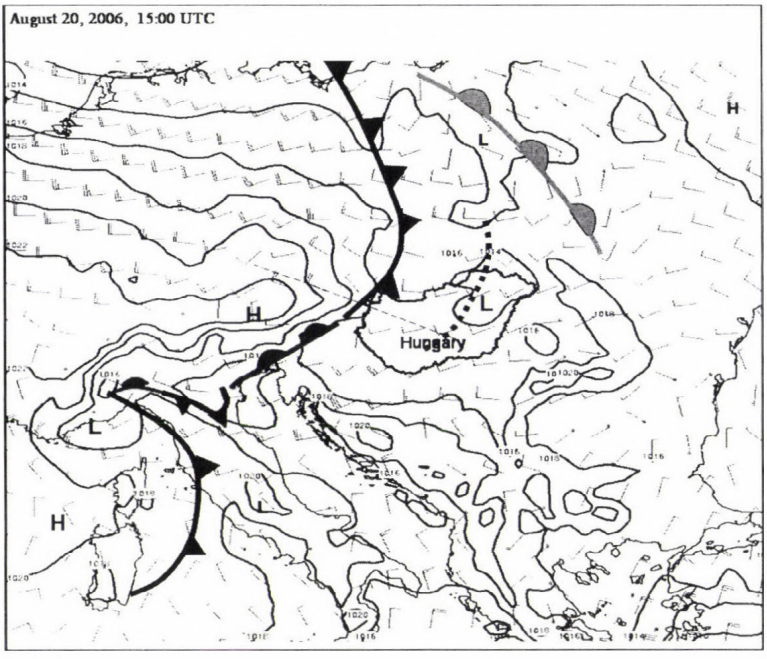

Fig. 1. ECMWF forecast of sea level pressure, 925 hPa wind, and fronts on August 20, 2006, 15:00 UTC. Dashed line shows the position of the direction of cross-section in Figs. 3 and 6.

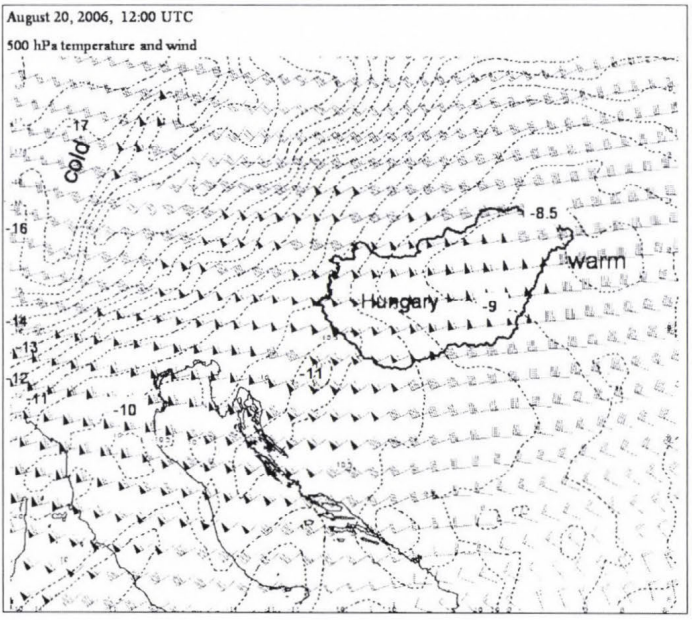

Fig. 2. 500 hPa wind and temperature (difference between the temperature isolines is 0.5 °C) on August 20, 2006, 12:00 UTC from the ECMWF analysis.

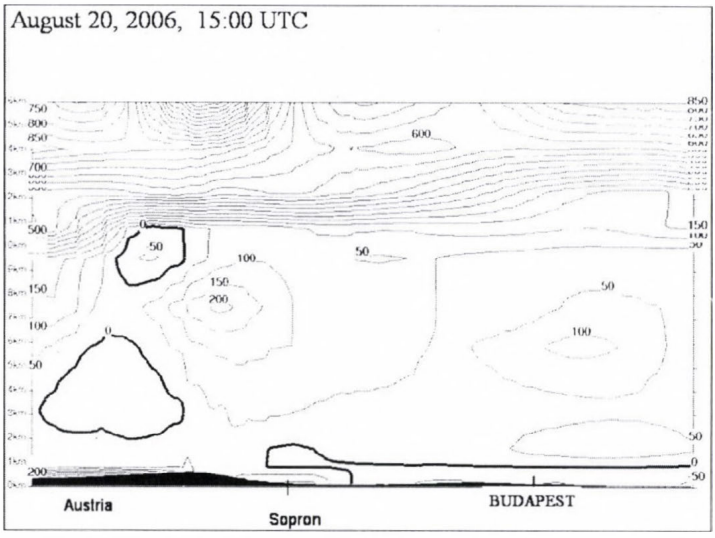

Fig. 3. Cross section of potential vorticity (10^{-5} s^{-1}) on August 20, 2006, 15:00 UTC from the ECMWF forecast. The direction of cross-section is denoted by dashed line in Fig. 1.

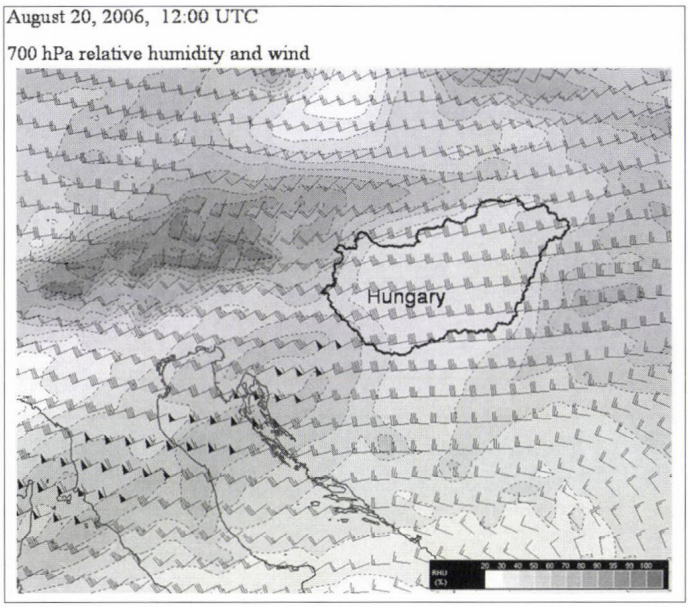

Fig. 4. 700 hPa wind and relative humidity on August 20, 2006, 12:00 UTC from the ECMWF analysis.

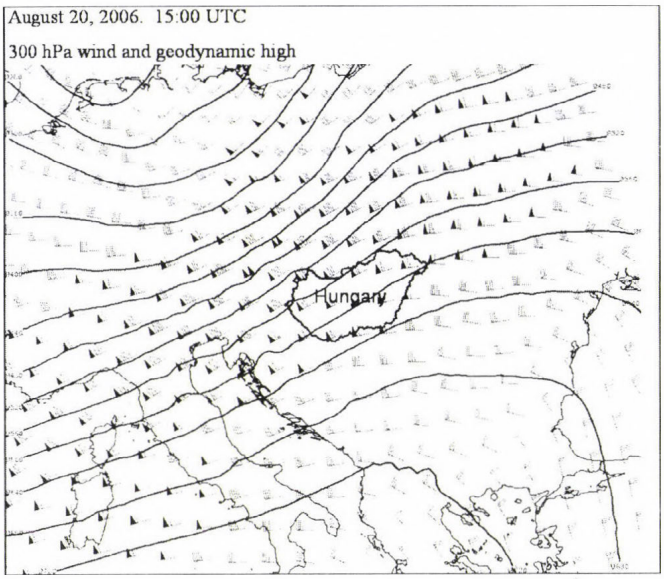

Fig. 5. 300 hPa wind and geopotentials on August 20, 2006, 15:00 UTC from the ECMWF forecast.

The direct role of the cold front in the formation of the Budapest storm is not obvious. Analysis of the ECMWF 12:00 UTC+6-hour forecast shows that the frontal system would not have reached Budapest by 19:00 UTC. The cross sections of potential vorticity and omega fields depict that the cold front reached the Hungarian border only at 18:00 UTC (*Fig. 6*). However observations show that the squall line was close to Budapest by this time.

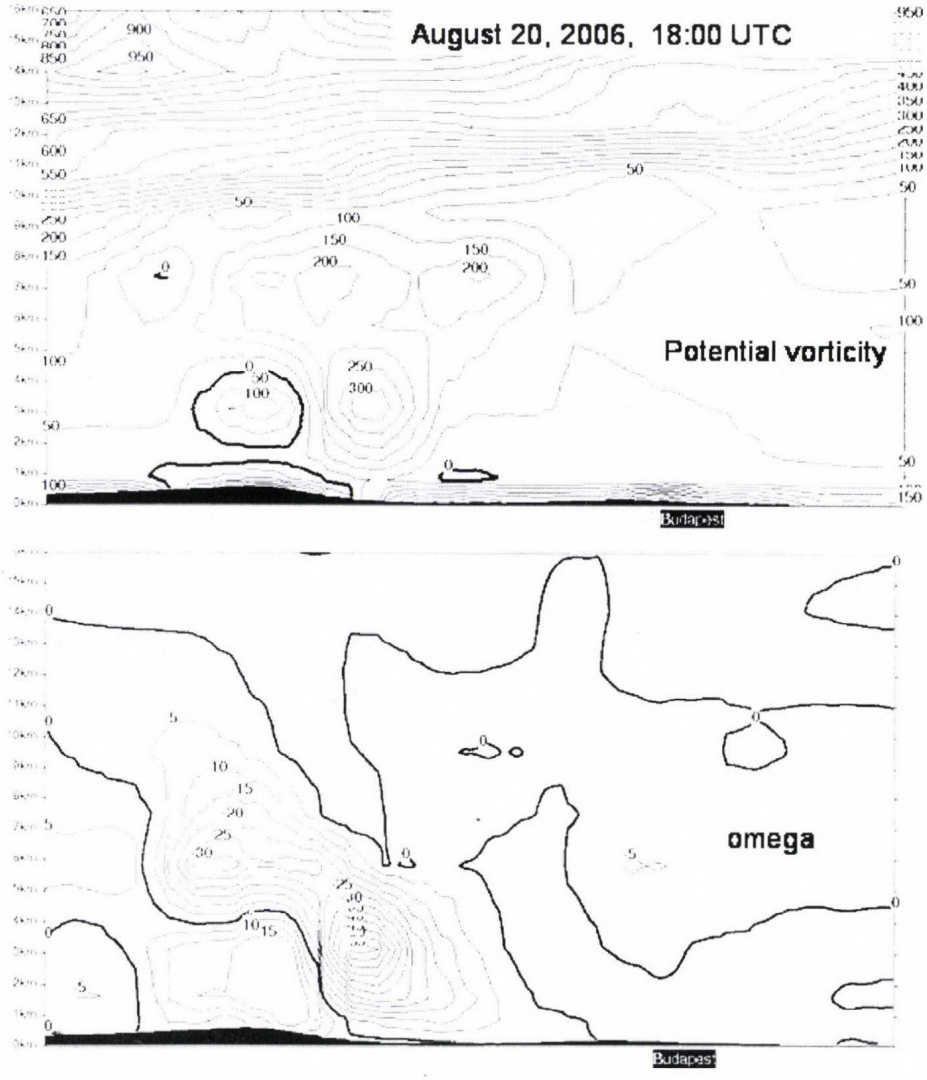

Fig. 6. Cross-section of potential vorticity (10^{-5} s^{-1}) and omega (10 Pa/h) at 18:00 UTC from the ECMWF forecast.

A possible explanation of the fact that thunderstorms arrived in Budapest 2 hours earlier than the modeled cold front is that a squall line separated from the front and run ahead. Because ECMWF forecast system is not suited for the simulation of convective scale processes, it was not able to predict the squall line. However it is notable that weather analysis could not distinguished different squall line and cold front in the time of Budapest storm.

Summing up the synoptic scale weather pattern in the investigated case one can state: (i) The wave of a sharp cold front formed an unstable warm sector, in which an intensive wet conveyor belt and strong high level jet stream resulted in favorable conditions for the formation of severe thunderstorms. (ii) After 15:00 UTC the effect of mesoscale convective processes became more dominant than that of the synoptic scale systems.

3. Observation of the Budapest storm

The HMS radar network detected the first significant radar echoes (R > 40 dBZ) at the eastern part of the Alps at 13:00 UTC. The line structure of the position of the thunderstorms could be observed at 13:45 UTC, still in Austria. The squall line reached the Hungarian-Austrian border at 16:30 UTC (*Fig. 7a*). This time the observed wind gusts were below 20 m/s. At 17:45 UTC three main thunderstorm systems could be distinguished along the squall line: the first one was in the northern part, the second was in the center, and the third was in the southern part (*Fig. 7b*). Some of the weather stations reached by the squall line reported 22 m/s wind gusts at this time. By 18:15 UTC the most intensive thunderstorms appeared in the north part of the squall line, the maximum reflectivity was near 55 dBZ in this region. The thunderstorms in the central region became weaker, and the thunderstorms in the southern region fell behind the squall line (*Fig. 7c*). By 19:00 UTC the thunderstorms in the northerly part remained active, and their reflectivity maximum was near 60 dBZ (*Fig. 7d*). The north part of the squall line reached Budapest when the thunderstorms were very intensive in it. Time series of radar images show that three of thunderstorm-centers have long-lived (>2 hours) comma like cells, and presumably these cells were supercells. The presence of the wall cloud in the photograph of Budapest storm shows some similarity to the supercell features. The maximum observed wind gust in Budapest was 34.1 m/s, but extent of damage suggests even higher maximum wind speeds. An eyewitness reported funnel cloud, but it was not confirmed. The thunderstorm system moved to southeast direction, and at about 30 km southeast of Budapest a 38.3 m/s wind gust was measured. After leaving Budapest the system remained active as long as it reached the line of the river Tisza.

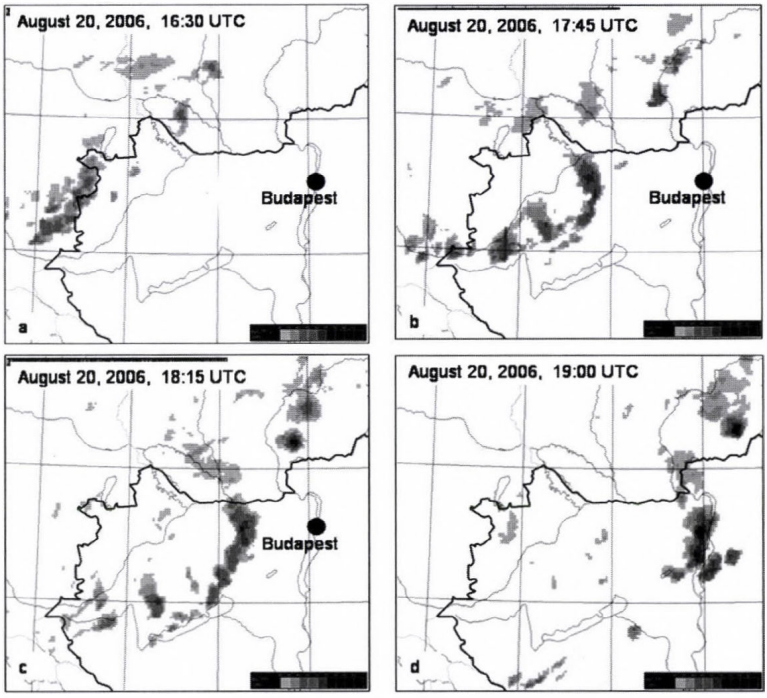

Fig. 7. Position of the squall line given by radar reflectivity.

3.1 Radar and lightening data

Thunderstorm formation and development were observed by the DWSR 2500 radar based weather radar network (3 radars) and SAFIR 3000 (7 sensors) based lightning location network of HMS. The data of these measurements were available in real time on the synoptic workstation of HMS all day. The basic radar and lightning characteristics were derived from the data of the routine observation, which include the national radar composites of CMAX dBZ values (maximum dBZ from 9 different elevations in every column) over a 800 km × 500 km region. The radar pictures were completed in every 15th minutes. The lightning events were recorded continuously this day providing data on IC and CG flashes. In our investigation these two data sets were carefully aligned in space and time. A site error compensation method was applied to reduce the large location errors of SAFIR system.

The radar and lightning data of the thunderstorms developed on August 20, 2006 did not show any unique or extreme characteristics. More intensive

thunderstorms were observed on 7 days in this year. The total amount of flashes and precipitable water produced by the thunderstorms on August 20 can be considered as typical summer values in Hungary.

The main characteristics are summarized in *Table 1* for lightning data (comparing to an extreme active lightning day) and *Table 2* for radar data.

Table 1. General lightning characteristics for August 3, 2005 (an extreme active day) and August 20, 2006

Date	Daily total			Maximum (15 min)		
	Localization	IC Flash	CG Flash	Density $km^{-2}\ h^{-1}$	Area km^2	Flashes
08.03.2005	532,375	242,301	40,405	34.5	17,552	28,808
08.20.2006	28,270	14,580	964	7.5	3656	3170
Ratio	**18.8**	**16.6**	**41.9**	**4.6**	**4.8**	**9.1**

Table 2. General radar characteristics on August 3, 2005 and on August 20, 2006

Date	Daily total			Maximum (15 min)			
	Water million m^3 >15 dBZ	Water million m^3 >45 dBZ	Mean rain >15 dBZ	dBZ	Area km^2 >15 dBZ	Water million m^3 >15 dBZ	Water million m^3 >45 dBZ
08.03.2005	2040,14	44,76	1.83	57.0	98,924	350,0	28,0
08.20.2006	915,88	112,06	2.97	59.5	38,940	15,0	33,0
Ratio	**2.2**	**0.4**	**0.6**	**-2.5**	**2.5**	**2.3**	**0.8**

Computer programs were developed to calculate different kind of characteristics of thunderstorm cells from radar and lightning data. These codes provide minimum and maximum values of dBZ, area and center points of the cells, as well as rainfall intensity and precipitable water content of every radar cell. The contour of the cells could be defined with different reflectivity thresholds. The composite radar picture was generated in every 15th minute. The number and maximum density of flashes, areas, center points are also calculated for flash cells at different density thresholds. Altogether 9 radar cells and 5 flash cells were identified and tracked. The tracked radar cells were defined with 35 dBZ reflectivity threshold, and their main parameters are shown in *Fig. 8.*

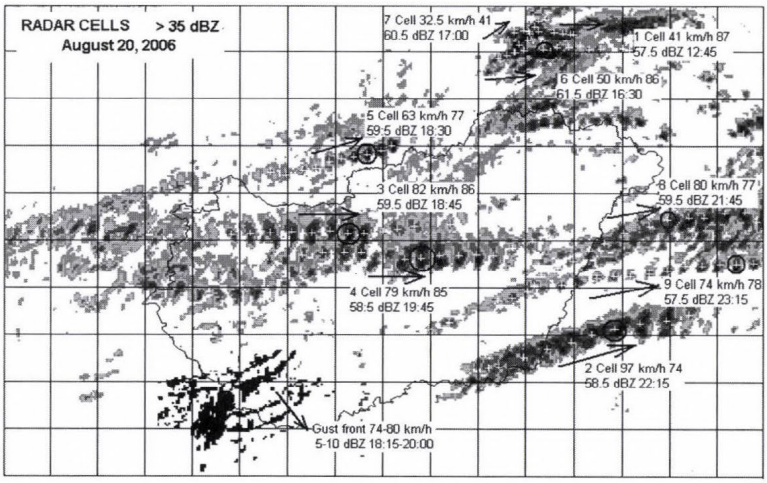

Fig. 8. The positions of the tracked radar cells in every 15th minute. The cells are defined with 35 dBZ reflectivity threshold. The main parameters are given: cell ID, mean velocity of motion, direction of motion (also with vectors), maximum reflectivity, and time of observation. The size of a grid is 50×50 km.

The main calculated parameters and features are shown in *Table 3* for radar cells and *Table 4* for flash cells. The cell ID used in figures and tables mark the same thunderstorm cells.

Table 3. Radar characteristics of thunderstorm cells on August 20, 2006

	Maximum reflectivity	**Time**	**Max. area**	**Total water**	**Mean velocity**	**Mean direction**	**Max. area**	**Max. water production**
	dBZ		**km^2**	**million m^3**	**km/h**	**degree**	**km^2**	**million m^3 h^{-1}**
Threshold			**15 dBZ**	**15 dBZ**	**35 dBZ**	**35 dBZ**	**35 dBZ**	**35 dBZ**
Cell ID								
1	57.5	12:45	788	21.9	40.7	86.8	428	13.7
2	58.5	22:15	9062	93.4	96.7	74.3	1404	44.4
3	59.5	18:45	2596	49.0	82.2	85.5	860	24.8
4	58.5	19:45	1153	50.9	78.5	84.3	738	30.1
5	59.5	18:30	805	23.0	62.7	76.9	689	13.6
6	61.5	16:30	759	26.2	50.1	86.0	496	19.0
7	60.5	17:00	532	14.7	32.5	41.2	280	12.2
8	59.5	21:45	2346	46.5	80.3	76.7	810	26.4
9	57.5	23:15	865	27.6	73.8	77.5	349	10.1

Table 4. Lightning characteristics of thunderstorm cells on August 20, 2006

	Max. flash density	Time	Max. area	Total flash	Mean velocity	Mean direction	Max. flash area	Max. flash activity
	$km^{-2}\ h^{-1}$		km^2		$km\ h^{-1}$	degree	km^2	h^{-1}
Threshold			$2\times km^{-2}\ h^{-1}$		$2\times km^{-2}\ h^{-1}$	$2\times km^{-2}\ h^{-1}$	$2\times km^{-2}\ h^{-1}$	
Cell ID								
2	28	21:15	1100	5187	96.6	92.4	668	5280
3	15	18:30	354	1313	81.7	86.7	216	1290
4	16	19:45	116	1156	91.6	106.0	64	560
5	12	18:15	176	429	62.0	71.6	76	492

In *Fig. 9* the water and flash production are shown for each tracked convective cells.

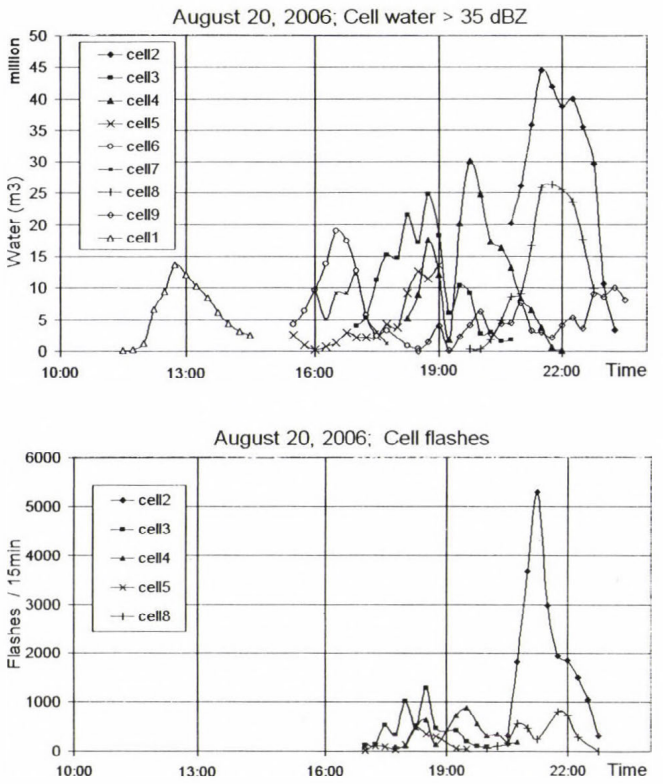

Fig. 9. The development of the water production (above) and the flash activity (below) in 15 minutes time intervals for each of tracked thunderstorm cell on August 20, 2006.

In *Table 5* the main radar and lightning characteristics of Budapest storm are summarized.

Table 5. Radar and lightning characteristics of Budapest thunderstorm cells on August 20, 2006

	Radar				Lightning			
	Max. dBZ	**Velocity**	**Direction**	**Area**	**Max. flash density**	**Velocity**	**Direction**	**Flash area**
	dBZ	**km h^{-1}**	**degree**	**km^2**	**km^{-2} h^{-1}**	**km h^{-1}**	**degree**	**km^2**
Thres.		**35 dBZ**	**35 dBZ**	**35 dBZ**		**2×km^{-2} h^{-1}**	**2×km^{-2} h^{-1}**	**2×km^{-2} h^{-1}**
Time								
17:00	43.0	0	0	388	6	0	0	60
17:15	50.5	83	82	268	4	172	123	102
17:30	52.5	79	90	538	7	88	85	276
17:45	52.5	86	87	648	4	92	71	196
18:00	53.5	89	75	648	10	144	99	444
18:15	55.5	77	89	780	9	28	146	274
18:30	55.0	74	101	802	15	80	85	354
18:45	59.5	76	84	860	7	64	76	188
19:00	57.0	81	93	598	SAFIR HMS stop			
19:15	46.5	screening		620	10	152	96	188
19:30	50.5	81	33	548	7	80	126	88

On the base of the radar and flash characteristics of tracked cells, the main features of the August 20 storm are the following:

- There was rapid eastward cell displacement this day. The velocity of the cells increased from 40 km/h (cell 1, at noon) to 82 km/h. The direction of motion turned slowly from the east to the north. Most of the thunderstorms involved two or more convective cells.
- The thunderstorm (cell 2) developed in the southeast region of the squall line and produced the maximum number of flashes at 21:15 UTC and precipitable water at 22:15 UTC. The total precipitable water was 94 million m^3, the maximum reflectivity was 58.5 dBZ, and the area of the largest cell was 9000 km^2.
- The most intensive thunderstorm (cell 3) moved almost eastward with a velocity of 82 km/h. The cell reached its maximum phase at 18:45 UTC with maximum reflectivity of 59.5 dBZ. This thunderstorm was composed of different convective cells producing about 49 million m^3 precipitation over a 2500 km^2 area.

- The Budapest storm was initiated by strong convection development at late afternoon in the west Hungary. This development resulted in a rapid gust front moving with about 74–80 km/h to the southeast. The observed reflectivity of the gust front was about 5–10 dBZ. The gust front was observed 1.5 hours ahead by the western radar of the network (Pogányvár C band radar).
- None of the radar cells, that have larger maximum radar reflectivity than 55 dBZ, showed observable flash activities.
- In every cell the flash activity reached its maximum value about 15–45 minutes earlier than the radar reflectivity and precipitable water production reached their maximum values.
- The velocity and the direction of motion of every cell were almost constant, or changed very slowly. This characteristic gave a chance for making forecasts of the cell positions 2–3 hours ahead.

In this research the existence of supercell was investigated by using objective methods. Doppler wind data were applied to find rotating cells using Rankine vortex theory (*Doviak* and *Zrnic*, 1993). The Rankine vortex (RV) model can be applied to recognize mesocyclones with characteristic size of 10 km. Tangential wind component (V_t) of the RV is given by the following equations:

$$V_t(r) = \frac{V_t^{\max}}{R_0} r \qquad \text{if} \quad r \le R_0,$$

$$V_t(r) = \frac{V_t^{\max}}{r} R_0 \qquad \text{if} \quad r > R_0,$$

where r is the distance from the center of RV, R_0 is the "radius" of the vortex, where the tangential wind has its maximum ($V_t^{\max}$).

Rankine vortex theory allows radial inflow or outflow (V_r) of the vortex:

$$V_r(r) = \frac{V_r^{\max}}{R_0} r \qquad \text{if} \quad r \le R_0,$$

$$V_r(r) = \frac{V_r^{\max}}{r} R_0 \qquad \text{if} \quad r > R_0,$$

where $V_r^{\max}$ is the maximum radial wind of the vortex at R_0. The vortex could be determined unambiguously, if the coordinates of the center of RV, $V_t^{\max}$ and $V_r^{\max}$, and R_0 were known. For the reason of simplicity,

transformation of radar measured Doppler wind field into storm relative coordinate system is applied. Rankine vortices between diameters of 2 and 10 km were searching in such a way, that all points were tested as a possible center of an RV. A real vortex has to satisfy the following conditions:

(i) Inside the vortex $\frac{\partial V_r}{\partial r} \geq 2.5 \frac{\text{m s}^{-1}}{\text{km}}$.

(ii) $2R_0$ is between 2 and 10 km.

(iii) The explained variance of the tested vortex and the Doppler wind in the storm relative coordinate system has to be higher than 80%.

The most significant RV structures of the Budapest storm were found at 19:11 UTC when Doppler radar scanned at 1° elevation angle (*Fig. 10*). One of the cyclonic rotation center was exactly above the downtown where the Constitution Day firework occurred.

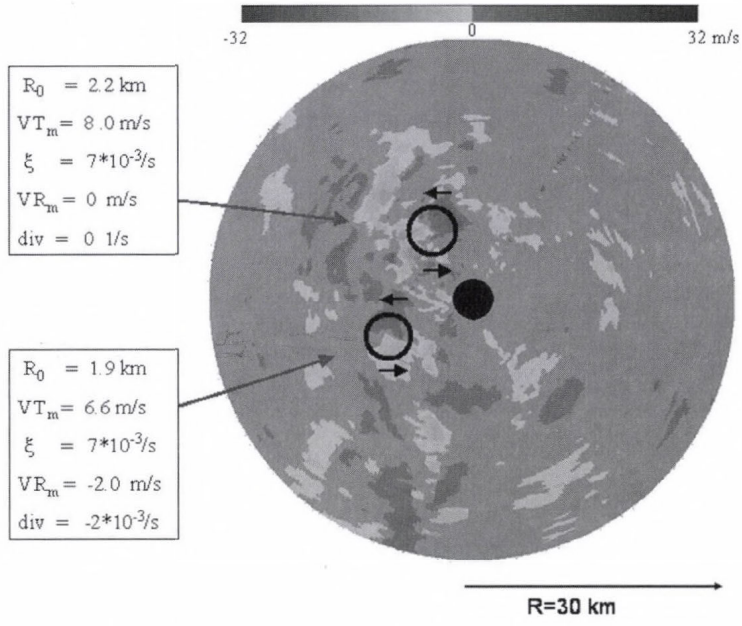

Fig. 10. Doppler wind field in storm relative coordinate system in 30 km radius of Budapest radar on August 20, 2006, 19:11 UTC. Circles show the indicated Rankine vortices with their parameters (ξ: vorticity; R_0: radius of the Rankine vortex; V_{tm}: tangential wind component of the vortex; V_{rm}: radial wind component of the vortex; div: divergence of the vortex). The northern vortex was above the downtown of Budapest.

4. Numerical simulation of the Budapest storm

The aim of the numerical model experiments was to understand the dynamics of thunderstorms like the Budapest storm and to investigate their predictability. The numerical simulations were made by the MM5 Version 3 (NCAR-PSU Mesoscale Model) (*Dudhia*, 1993). The high horizontal resolution (1.5 km) allowed us to run the model without cumulus parameterization. To describe microphysical processes, Reisner microphysical scheme (with five different types of hydrometeors) is applied (*Reisner et al.*, 1998). The planetary boundary layer (PBL) is described by the non-local PBL scheme based on *Troen* and *Mahrt* (1986). Land-surface processes are simulated by the Oregon State University Land-surface Model (*Chen* and *Dudhia*, 2001). For this study, the model was integrated with horizontal resolutions of 1.5 km, with 28 vertical levels on 400×500 horizontal grid points. 100 hPa was chosen as the upper level of the model. The model domain was chosen in such a way that the cold front was in the inner part of the model territory at 12:00 UTC initial time. A Lambert-conformal projection was applied with 48.0° latitude and 16.4° longitude central values. An experimental model run with 12 hours forecast needed 4 hours computer time on 64 processors of an ALTX 3700b computer.

The initial and lateral conditions for the MM5 were taken from the ECMWF deterministic model run of 12:00 UTC, on August 20. The ECMWF data set has 0.25 degree resolution. The MM5 model run initiated at 12:00 UTC used the 12:00 UTC ECMWF analysis. The other runs initiated at 13:00 and 14:00 UTC used +1 and +2 hours ECMWF forecast for initial conditions. Input data for MM5 initial condition (mean sea level pressure, three-dimensional temperature, humidity, wind fields, soil temperature and soil humidity values) were taken from the ECMWF analysis.

During model experiments at model run of 14:00 UTC, reflectivity of HMS radar network were also assimilated into initial conditions using the Robust Radar Impact (RRI) method (*Horváth*, 2006). The RRI method is based on theory and numerical experiments which show that the vertical profile of equivalent potential temperature (EPT) can be considered as a nearly constant value, especially in the cases of severe thunderstorms. Supposing that the air in thunderstorms is saturated (relative humidity profile is 100%), it is possible to retrieve a pressure-temperature profile which is valid only in the updraft regions of thunderstorms. In this way thunderstorms appear like warm and wet bubbles isolated from their environment. Case studies were made to determinate the most efficient way to calculate the characteristic EPT value. It was found that EPT of the most unstable layer of the lowest 1000 meters can be considered characteristic for air mass thunderstorms.

A new subprogram which calculates the reflectivity of the precipitation elements (rain, snow, and hail/graupel) was attached to the original code of the MM5. The calculated radar reflectivity field allows us to make a more direct comparison with the radar observation. (The quantitative comparison between the simulated precipitation intensity and the precipitation intensity derived from the reflectivity is very limited, because the calculation of precipitation field from the radar data bases on crude approximations.) The difficulty of the reflectivity calculation can be handled by supposing that the size of the precipitation elements is small enough to fall into the Rayleigh scattering region, and that the size distributions of these particles are given by an exponential function with fixed intersection parameters. According to *Smith et al.* (1975) the effect of the Mie-theory can be neglected, because the concentration of the hail stones larger than the radar wavelength (3–10 cm) is very small. The dielectric factor of 0.93 and 0.21 were used for the water drops and dry ice particles, respectively. If the temperature is larger than 0°C, the dielectric factor of the ice particles is the same as that of the water drops, because in this case a thin water layer formed on the surface of the ice particles.

3.1 Results of numerical experiments

Several numerical model experiments were made to determinate the optimal model domain and initiation time. A simulation was considered to be successful, if a thunderstorm with mesoscale rotation (mesocyclone) appeared during the simulation. All simulations predicted the cold front passage between 18:00 and 21:00 UTC in Budapest, but severe convective phenomena and associated mesocyclones appeared only in the cases, when at the start of the simulation the cold front was inside the model domain. In cases when the cold front only drifted into the model domain due to the lateral conditions (given by the ECMWF forecast), the model was not able to forecast mesocyclones. In runs with initial times later than 15:00 UTC, the model was not able to develop mesocyclones by 19:00 UTC.

The model run with 12:00 UTC initial time forecasted the squall line and some mesocyclones appeared in the line. However, the dominant supercell moved south of Budapest, and the simulated squall line reached the Danube one hour earlier than in real case. In this case the RRI method was useless, because at the initial time the radar echoes were weak. The most successful model run was when 14:00 UTC initiation was applied. In this case the RRI method helped the model to involve triggers to the appropriate places and passage, and the development of the squall line were closest to reality. Hereafter the results of the 14:00 UTC model run are discussed.

The calculated radar reflectivity seemed to be a good parameter to compare the model simulation with the measured radar data. The model retrieved a realistic image of the real squall line by 15:00 UTC (1 hour forecast), which means that the spin up time was less than one hour. The modeled squall line reached the Austrian-Hungarian border at the same time when the real squall line did. At 17:45 UTC three main calculated reflectivity maxima can be seen in *Fig. 11a*. Detailed analysis indicates that all of the three centers had mesocyclone. At this time the southern center had the strongest mesocyclone. At 18:15 UTC already the northern center had the highest reflectivity values and the southern center dropped behind (*Fig. 11b*), while at 18:45 UTC the northern center became obviously the dominant system (*Fig. 11c*). The squall line reached the Danube at 19:15 UTC only 15 minutes later than the real storm did (*Fig. 11d*). A detailed picture of the wind field and the calculated radar echoes show the center of the mesocyclone, which is only a few kilometers from the downtown of Budapest (*Fig. 12*).

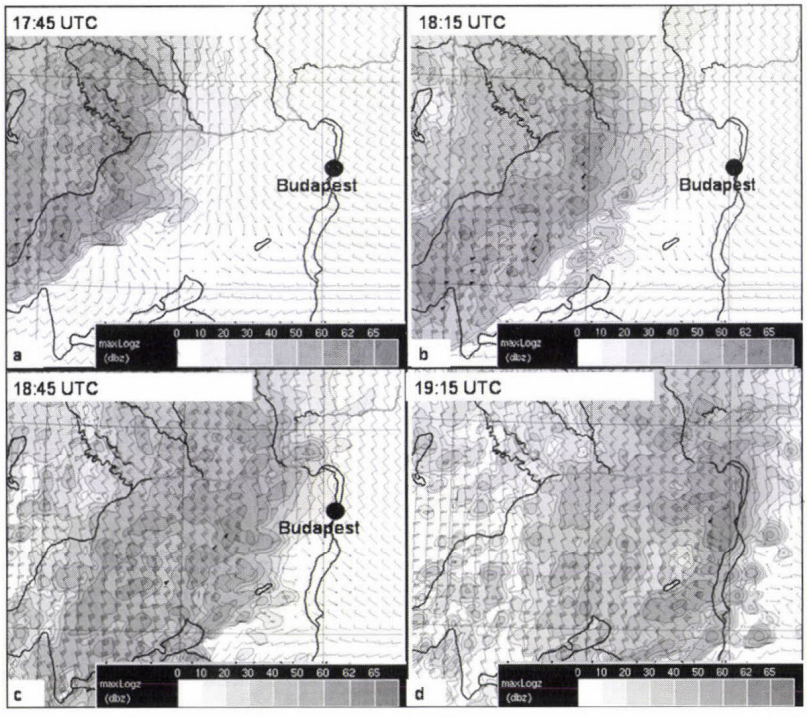

Fig. 11. MM5 simulated radar reflectivity (shadowed fields) and 925 hPa wind field of the squall line passage.

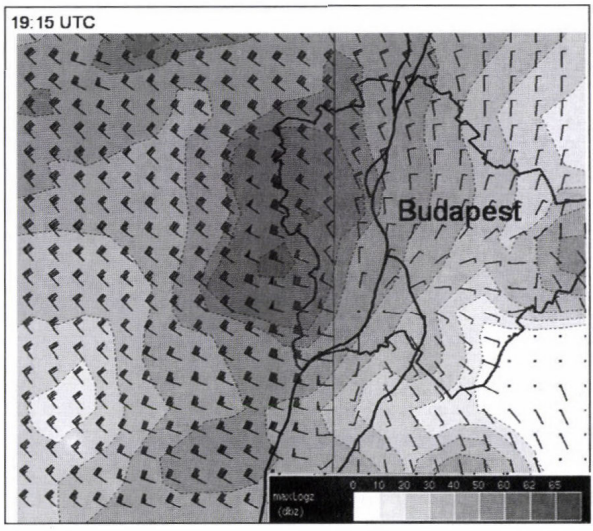

Fig. 12. MM5 simulated radar reflectivity and 925 hPa wind field at 19:15 UTC.

The low level thermodynamic characteristics of the squall line are shown by wind and equivalent potential temperature (EPT) fields of the 925 hPa level (*Fig. 13a, b*). The first conspicuous feature is that EPT values rise up behind the leading edge of the squall line. This behavior is opposite to that was found in an earlier investigated supercell occurred in Hungary (*Horváth et al.*, 2006). In this case the thunderstorms collected low level unstable air from areas in front of the thunderstorm line, and behind the thunderstorms EPT field formed a cold pool. At the present case the low level pattern of EPT suggests that low level prefrontal instability did not play an important role in supplying of the squall line. Missing of significant cold pools behind the squall line also supports this assumption.

The low level thermodynamic characteristics of the squall line are shown by wind and equivalent potential temperature (EPT) fields of the 925 hPa level (*Fig. 13a, b*). The first conspicuous feature is that EPT values rise up behind the leading edge of the squall line. This behavior is opposite to that was found in an earlier investigated supercell occurred in Hungary (*Horváth et al.*, 2006). In this case the thunderstorms collected low level unstable air from areas in front of the thunderstorm line, and behind the thunderstorms EPT field formed a cold pool. At the present case the low level pattern of EPT suggests that low level prefrontal instability did not play an important role in supplying of the squall line. Missing of significant cold pools behind the squall line also supports this assumption.

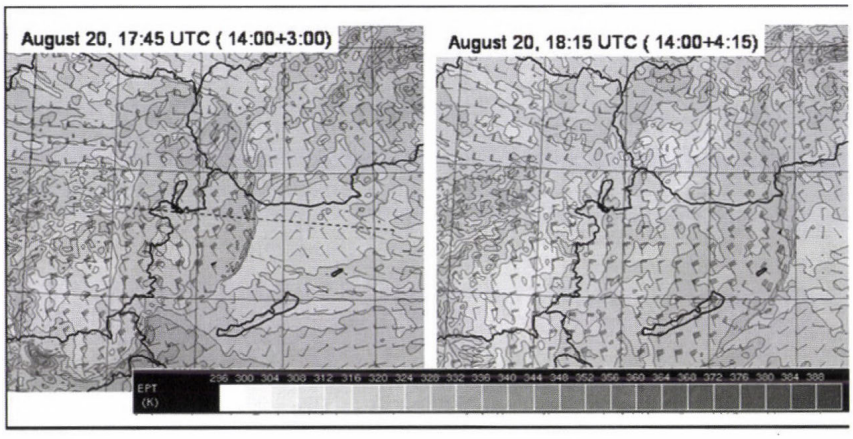

Fig. 13. MM5 simulated equivalent potential temperature and wind field on the 925 hPa level. Dashed line shows the position of cross-section in Fig. 14.

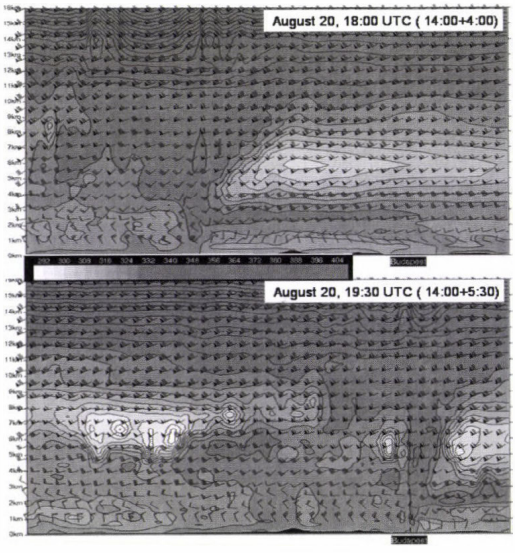

Fig. 14. Cross-section of MM5 simulated equivalent potential temperature and wind field during the squall line passage. The direction of the squall line is shown in Fig. 13.

Vertical cross sections of the squall line suggest that the unstable air mass which supplied the line of thunderstorms is between 1.5 and 4 km AGL (*Fig. 14a*). This unstable layer is generated by an active wet conveyor belt on the

700 hPa level. (More details about the wet conveyor belt are given at synoptic conditions in Section 2). The cold layer between the 5 and 7 km heights was a consequence of high level cold advection. This layer was responsible for the prefrontal conditional instability. The cold advection on the 500 hPa level was presented at discussion of the synoptic conditions in Section 2. The squall line can be identified by the towering maximum of EPT up to the troposphere and by lower level directional wind shear (*Fig. 14a, b*). Several parameters were used to analyze the cold front and to separate the front from the squall line. The cross section in *Fig 14b* shows low level cold advection behind the squall line, but there is no significant wind shear (both direction and speed) which would unambiguously indicate the cold front. An option is that the squall line probably blurred the cold front behind itself. The other option is that the squall line accelerated the front, and the separating line between the cold and warm air mass, and the squall line were identical.

5. Conclusion

The Budapest storm was not a classical self propagation squall line, where the cold pool and the low level wind shear play the main role in the formation of line of thunderstorms (*Rotunno*, 1982). The storm can not be place into the certain category of cold front aloft, where high level cold front is responsible for line organized convective storms (*Stoelinga et al.*, 2003). However, the situation was similar to a certain degree.

Basic conditions for convective instability were provided by synoptic scale events and weather patterns. The long frontal system extending across the continent provided good conditions for producing a significant prefrontal wet conveyor belt on the 700 hPa level. This layer supplied convective energy, instead of relative cold and stable lower air, allowing the formation of nocturnal thunderstorms. The frontal wave formed at the southeast Alps caused the air masses to slow down at low level and to run ahead at high level, above the warm sector. Also that wave was responsible for wind shear favorable for supercell formation.

In the unstable prefrontal warm sector a squall line developed and the thunderstorms which hit Budapest were parts of the squall line. The squall line had three main storm centers and by the time of reaching Budapest, the northerly center became the strongest.

Concerning radar reflectivity and lightning activity, the storm and the squall line were not extreme strong events, however, cell motions were very fast. Detailed Doppler wind analysis showed that among cells, which hit Budapest, there were supercells. In spite of the existence of supercells, the

typical left or right deviation from the leading squall line direction was not recognized by detailed cell tracking analysis. The extreme fast motion was not favorable for supercell splitting.

High resolution, non-hydrostatic model experiments successfully simulated the squall line and the rotating thunderstorms in time and space. Model results show that thunderstorms got air masses with high equivalent potential temperature from layers between 2–4 km AGL. The air mass near the surface layers were stable, and did not supplied thunderstorms.

The fast moving squall line resulted in that the storm arrived in Budapest about a few hours earlier than the synoptic scale cold front was predicted. Even detailed analysis can not answer obviously, whether the squall line was a prefrontal phenomenon or the cold front became faster because of strong convection, but the direct role of the cold front at the Budapest storm is evident.

Acknowledgement—This research was supported by the NKFP 0022/2005 (Jedlik Ányos) project.

References

Bartha, I., 1987: An objective decision procedure for prediction of maximum wind gusts associated with Cumulonimbus clouds. *Időjárás 91*, 330-346.

Bodolainé, J.E. and *Tänczer, T.*, 2003: *Mesoscale Convective Systems - Triggering Off Flash Floods* (in Hungarian). Országos Meteorológiai Szolgálat, Budapest.

Böjti, B., Bodolainé, J.E., and *Götz, G.*, 1964: Instability lines in Hungary (in Hungarian). *Beszámolók az 1964-ben végzett tudományos kutatásokról*. Országos Meteorológiai Szolgálat, Budapest, 139-165.

Chen, F. and *Dudhia, J.*: 2001: Coupling and advanced land surface-hydrology model with the Penn State-NCAR MM5 modeling system. Part I. Model implementation and sensitivity. *Mon. Weather Rev. 129*, 569-585.

Davies-Jones, R., Trapp, R.J., and *Bluestein, H.B.*, 2001: Tornadoes and tornadic storms. In *Severe Convective Storms* (ed.: *C.D. Doswell*). *AMS Meteorological Monographs 28*, No. 50, 167-221.

Doviak, R.J. and *Zrinic, D.S.*, 1993: *Doppler Radar and Weather Observations*. Academic Press, 335-340.

Dudhia, J., 1993: A non-hydrostatic version of the Penn State-NCAR Mesoscale Model: Validation tests and simulation of an Atlantic cyclone and cold front. *Mon. Weather Rev. 121*, 1493-1513.

Fujita, T.T., 1955: Results of detailed synoptic studies of squall lines. *Tellus 7*, 405-436.

Fujita, T.T., 1959: Precipitation and cold air production in mesoscale thunderstorm systems. *J. Meteor. 15*, 454-466.

Geresdi, I. and *Horváth, Á.*, 2000: Nowcasting of precipitation type. Part I: Winter precipitation. *Időjárás 104*, 241-252.

Geresdi, I., Horváth, Á., and *Mátyus, Á.*, 2004: Nowcasting of the precipitation type Part II: Forecast of thunderstorms and hailstone size. *Időjárás 108*, 33-49.

Götz, G., 1966: *Sturmwarnung am Balatonsee* (in German). Országos Meteorológiai Szolgálat, Budapest.

Götz, G., 1968: Hydrodynamic relationships between heavy convection and the jet stream. *Időjárás 72*, 157-165.

Holton, J.R., 2004: *An Introduction to Dynamic Meteorology*. Elsevier Academic Press.

Horváth, Á.,1997: Tornado (in Hungarian). *Légkör 62*, 2-9.

Horváth, Á., 2006: Numerical studies of severe convective phenomena using robust radar impact method. In *Proceedings of ERAD 2006*. Barcelona, 19-22 September, 557-558.

Horváth, Á. and *Práger, T.*, 1985: Study of dynamic and predictability of squall lines (in Hungarian). *Időjárás 89*, 141-160.

Horváth, Á. and *Geresdi, I.*, 2003: Severe storms and nowcasting in the Carpathian Basin. *Atmos. Res. 67-68*, 319-332.

Horváth, Á., Geresdi, I., and *Csirmaz, K.*, 2006: Numerical simulation of a tornado producing thunderstorm: A case study. *Időjárás 104*, 279-297.

Hoskins, B.J. and *Bretherton, F.P.*, 1972: Atmospheric frontogenesis models: Matematical formulation and solution. *J. Atmos. Sci. 29*, 11-37.

Houze, R.A., Rutledge, S.A., Biggerstaff, M.I., and *Sull, B.F.*, 1989: Interpretation of Doppler weather radar displays in middle latitude mesoscale convective systems. *B. Am. Meteorol. Soc. 70*, 608-619.

Klemp, J.B. and *Wilhelmson, R.*, 1978: The simulation of three dimensional convective storm dynamics. *J. Atmos. Sci. 35*, 1070-1096.

Klemp, J.B., 1987: Dynamics of tornadic thunderstorms. *Ann. Rev. Fluid Mech. 19*, 369-402.

Lilly, D.K., 1962: On the numerical simulation of buoyant convection. *Tellus XIV*, 148-172.

Reisner, J., Rasmussen, R.M., and *Bruintjes, R.T.*, 1998: Explicit forecasting of supercooled liquid water in winter storms using the MM5 mesoscale model. *Q. J. Roy. Meteor. Soc. 124*, 1071-1107.

Reynolds, D.A. and *Smith, E.*, 1979: Detailed analysis of composited digital radar and satellite data. *B. Am. Meteorol. Soc. 60*, 1024-1037.

Rotunno, R., Klemp, J.B., and *Weisman M.L.*, 1988: A theory for long living squall lines. *J. Atmos. Sci. 45*, 463-485.

Shapiro, M.A., 1982: *Mesoscale Weather Systems of the Central United State*. University of Colorado, Boulder, Co.

Smith, P.L., Jr., Myers, C.G., and *Orville, H.D.*, 1975: Radar reflectivity factor calculations in numerical cloud models using bulk parameterization of precipitation. *J. App. Meteorol. 14*, 1156-1165.

Stoelinga, M.T., Locatelli, J.D., Schwartz, D.R., and *Hobbs, P.V.*, 2003: Is a cold pool necessary for the maintenance of a squall line produced by a cold front aloft? *Mon. Weather Rev. 131*, 95-115.

Troen, I. and *Mahrt, L.*, 1986: A simple model of the atmospheric boundary layer: Sensitivity to surface evaporation. *Bound.-Lay. Meteorol. 37*, 129-148.

Wilhelmson, R.B. and *Wicker, L.J.*, 2001. Numerical modeling of severe local storms. In *Severe Convective Storms* (ed.: *C.D. Doswell*). *AMS Meteorological Monographs 28*, No. 50. 123-166.

Zoltán, Cs. and *Geresdi, I.*, 1984: A one-dimensional steady-state jet model for thunderclouds. *Időjárás 88*, 21-31.

IDŐJÁRÁS

Quarterly Journal of the Hungarian Meteorological Service
Vol. 111, No. 1, January–March 2007, pp. 65–77

Crop growing periods and irrigation needs of corn crop at some stations in Northeast Brazil

K. Karuna Kumar* and **T.V. Ramana Rao**

Department of Atmospheric Sciences, Federal University of Campina Grande
58.109-970 - Campina Grande – PB, BRAZIL
E-mail: karuna@dca.ufcg.edu.br

(Manuscript received in final form October 23, 2006)

Abstract—Results of a climatological study of soil moisture under corn crop at six stations in the semiarid region of Northeast Brazil are reported in this paper. Daily values of available soil moisture during the wet season are evaluated using a six-zone versatile soil moisture budget (VSMB) model. A first order Markov chain model is applied to the daily soil moisture data. Soil moisture averages and probabilities are used to identify the optimum growing periods for corn crop at the stations, and the irrigation needs during these periods are evaluated. The effect of soil hydro physical properties in the VSMB model is discussed. The use of mean daily precipitation values in the model in place of actual precipitation data is briefly discussed.

Key-words: versatile soil moisture budget, available soil moisture, crop growing periods, irrigation needs, Markov chain probabilities

1. Introduction

Soil moisture is an important parameter in agriculture, forestry, and hydrology. It plays a significant role in determining crop yields and in the hydrological balance of a region. Since it is impractical to measure soil moisture on the time and space scales required for agro-climatological studies, several models have been developed in the past for its estimation (*Thornthwaite* and *Mather*, 1955; *Holmes* and *Robertson*, 1959; *Baier* and *Robertson*, 1966; *De Jong* and *Shaykewich*, 1981; *Robertson*, 1985). The versatile soil moisture

*Address for correspondence: R. Rodrigues Alves 1183, Apt 203, Prata Campina Grande – 58101-291 (PB), BRAZIL

budget (VSMB) originally developed by *Baier* and *Robertson* (1966) takes into consideration the rooting depth of the crop, root concentration in different soil zones, and water holding and water release characteristics of each zone. In addition, allowance can be made for the changes in root concentration, as the crop develops towards maturity.

De Jong (1988) compared the soil moisture estimates from the VSMB and SPAW (soil-, plant-, air-water) models with measured data in the semiarid region of Saskatchewan. He found that both models gave equally good results, and that the VSMB model required less crop and soil information as input than the SPAW model. *Boisvert et al.* (1992) used the VSMB model to predict the water table depth. It has also been used to study the soil moisture conditions in the Canadian prairies (*De Jong et al.*, 1992). The VSMB model has been used to estimate soil moisture under palm plantations in Malaysia (*Robertson* and *Foong*, 1977), to calculate soil moisture in arid soils in India (*Robertson*, 1977), and to predict summer drought conditions under grass land in South Africa (*Dyer* and *De Jager*, 1986). Recent developments in soil water modeling including the VSMB model were reviewed by *De Jong* and *Bootsma* (1996) and *Baier* and *Bootsma* (1999).

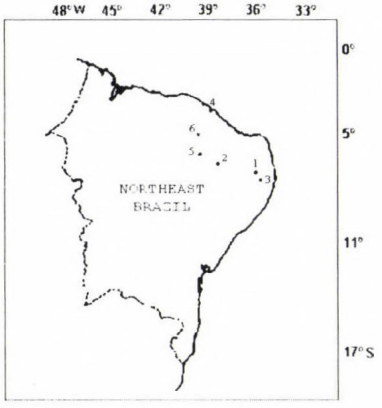

Fig. 1. Location of stations. 1. Campina Grande; 2. São Gonçalo; 3. Umbuzeiro; 4. Fortaleza; 5. Iguatu; 6. Quixeiramobim.

The present paper is based on a study of soil moisture conditions under corn crop at six stations in the semiarid zone of Northeast Brazil (*Fig. 1*). Northeast Brazil comprises an area of about 1.5 million km^2 and consists about 30% of the country's population. In the coastal areas rainfall can be up to 2000 mm per year. About 35% of the region lies in the zone of equatorial climate and 65% in the zone of subtropical climate. The highest and lowest recorded temperatures are 41.5 °C and 11.6 °C, respectively. About 10% of the region receives less than 250 mm of annual rainfall and about 60% receives more than

600 mm. Apart from the generally low amount of rainfall, the highly irregular nature of rainfall during the year is responsible for the frequent occurrence of droughts in this region. In most years about 90% of annual rainfall occurs from December to April or May. The duration of the rainy season is fairly constant, but its starting point, which generally coincides with the sowing time, may vary between 60 to 90 days.

The semiarid zone occupies 60% of Northeast Brazil and contains 40% of its population. The main climatic characteristics are: annual rainfall of 400–800 mm with a high coefficient of variability, high air temperatures, and high potential evapotranspiration rates (averaging 2000 mm). The crops grown in the semiarid zone are cotton, corn, and beans.

In the semiarid zone the main constraint to crop production is rainfall and its extreme variability. Studies of soil moisture conditions under agricultural crops are thus a matter of much importance in this region.

2. Methodology

In the present study, long term mean decadal (ten day periods) potential evapotranspiration (*PE*) values derived from Thornthwaite's procedure (*Thornthwaite*, 1948, *Thornthwaite* and *Mather*, 1957) are used to obtain daily *PE* values, and these together with daily precipitation data are used to evaluate daily soil moisture values. A versatile soil moisture budget model is used for this purpose, and the computations are carried out for a minimum period of 25 years. Values of 75, 100, 150, and 200 mm are assigned to the available moisture capacity (*AWC*) of the root zone of the soil. The *AWC* is defined as the difference between the field capacity and the permanent wilting point. The soil root depth is divided into six zones and approximately 5, 7.5, 12.5, 25, 25, and 25% of the total *AWC* are attributed to zones one to six respectively.

The contribution of each zone to the total actual evapotranspiration (*AE*) is evaluated from following expression:

$$PAE_{j,x} = K_{i,j}\left(WS_{j,x-1} / WC_j\right) Z_{j,x} PE_x, \tag{1}$$

where $PAE_{j,x}$ = partial evapotranspiration from the jth zone on day x;
$K_{i,j}$ = crop coefficient for the jth zone in growth stage i;
$WS_{j,x-1}$ = available moisture content of the jth zone at the end of day $x-1$;
WC_j = available moisture capacity of jth zone;
PE_x = potential evapotranspiration on day x;
Z = factor depending on soil dryness characteristics.

A set of 100 values between 0.0 and 1.0 are assigned to Z corresponding to 100 values between 0.0 and 1.0 of WS/WC on the assumption, that the ratio AE/PE remains equal to unity until relative available moisture content WS/WC decreases to 0.7 and then decreases linearly with WS/WC. Such an assumption is a reasonable first approximation for most medium textured soils.

The K coefficients reflect the root activity at different depths during different growth stages of the crop. The corn crop-growing period is divided into three principal stages, and in each stage different K values are assigned to the six zones. When the upper zones of the soil are dry, relatively more moisture is removed from the lower zones than in the case of uniformly wet soil. To take this aspect into consideration, the K coefficients for each zone below the first are increased as a function of the moisture content of the respective upper zones.

$$K'_j = K_j + K_j \left[\sum_{m=1}^{j-1} K_m \left(1 - \frac{WS_m}{WC_m} \right) \right], \tag{2}$$

where K'_j = adjusted K coefficient for the jth zone;
WS_m = available moisture content in the mth zone;
WC_m = available moisture capacity of the mth zone;

The available moisture content and the moisture loss from each zone are obtained from the following expressions:

$$\begin{aligned} WS_{j,x} &= WS_{j,x-1} - PAE_{j,x}, \\ WS_{j,x} &= 0 \text{ if } PAE_{j,x} > WS_{j,x-1}, \end{aligned} \tag{3}$$

where $WS_{j,x}$ is the available moisture in the jth zone at the end of day x.

$$\begin{aligned} AE_{j,x} &= PAE_{j,x} \text{ if } PAE_{j,x} \leq WS_{j,x-1}, \\ AE_{j,x} &= WS_{j,x-1} \text{ if } PAE_{j,x} > WS_{j,x-1}. \end{aligned} \tag{4}$$

The sum of $AE_{j,x}$ for the six zones gives the actual evapotranspiration (AE) on day x. The sum of $WS_{j,x}$ for the six zones represents the available moisture content of the root zone of the soil on day x, if no precipitation occurs on that day. If precipitation occurs the values of $WS_{j,x}$ for some or all the six zones will increase.

On days with precipitation it is assumed, that moisture loss due to evapotranspiration occurs before precipitation. Precipitation enters the first zone and if this zone reaches its moisture holding capacity, the excess water

enters the second zone, and so on. Excess water leaving the sixth zone is considered the water surplus on that day.

In each year the computations are carried out for different four-month corn growing periods for the four *AWC* values assumed.

Each month is divided into three decades, the last decade having 8, 9, 10, or 11 days depending on the month. Based on the daily soil moisture data for the study periods, mean decadal available moisture contents are obtained. A first order Markov chain model is applied to the daily soil moisture data, and the initial and conditional probabilities of dry and wet days are computed. The critical moisture content separating a wet day from a dry day is taken to be half of the assumed *AWC* value. For each decade during the growing period, the probability of occurrence of five consecutive wet days, *P*(5W) is evaluated using the above probabilities. Soil moisture averages and probabilities are used to determine the optimum growing periods for corn at the stations.

The soil moisture model described above is also used to evaluate the irrigation needs for corn crop at the stations. The computations for *AWC* values of 100, 150, and 200 mm are repeated with the modification, that each time the available moisture content decreases to a predetermined value, the moisture content on that day is replaced with that corresponding to 95% of the *AWC*. In practical terms this means, that each time the soil moisture is depleted to a preselected value, irrigation is applied to bring it back to a safe level. This part of the study is carried out assuming three limiting soil moisture levels (50%, 70%, and 90% of the *AWC*). The number of irrigation applications during the four-month (optimum) growing period and the mean interval between irrigations are obtained for each year, and from these numbers the mean values for the study period are derived.

3. Results and discussion

Mean decadal values of available moisture content at Campina Grande are evaluated for different growing periods during the wet season for the four *AWC* values considered and results for AWC_{200} are shown in *Fig. 2*. It is found that in general, the available moisture content as a fraction of *AWC* decreases with the increase in *AWC* value from 75 to 200 mm. During the period May–August, available moisture content was almost always more than 50% of the *AWC* even though the climatic water balance based on Thornthwaite's procedure (*Thornthwaite*, 1948; *Thornthwaite* and *Mather*, 1957) shows large water deficiency during the months August-September. Based on mean decadal values of available moisture content, the period May–August is found to be the optimum growing period for corn at Campina Grande. Values of probability of

occurrence of five consecutive wet days, $P(5W)$ are evaluated for each of the twelve decades in successive four-month periods. The results once again indicate that the period May–August is the best of the three growing periods considered. The same conclusion is drawn on the basis of *Table 1*, which shows the available moisture content, exceeded at different probability levels. However, even during the period May–August, supplementary irrigation is found necessary for corn growth.

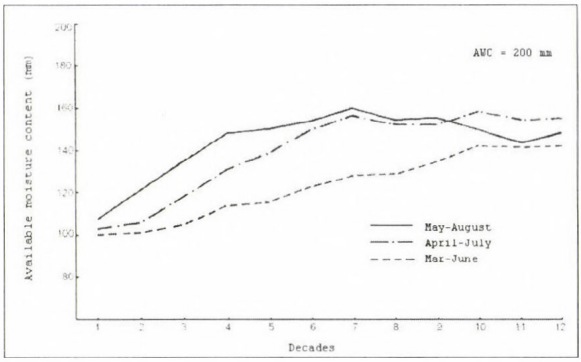

Fig. 2. Available soil moisture at Campina Grande in different growing periods.

Mean decadal values of *AE* for the months February–May for the 25-year study period at Teresina are compared with the corresponding *PE* values. During February, March, and May, *AE* is much smaller than *PE*. In April the moisture content in the root zone is quite high, and the sum of the *K* coefficients for the six soil layers is more than unity. Hence, *AE* during the three decades in April exceeds the *PE*. Under well watered conditions, *AE* estimates from the VSMB model exceed *PE* during a part of the growing cycle (*Dyer* and *Mack*, 1984). This in turn implies values of crop coefficient K_c, which relates evapotranspiration to reference crop evapotranspiration (*Doorenbos* and *Pruitt*, 1977) higher than 1. Values of K_c for corn between 1.0 and 1.2 during certain growth stages have been reported by *Allen et al.* (1998) and *Doorenbos* and *Kassam* (1979).

One of the parameters of the VSMB model is the *Z* factor, which is the ratio between *AE/PE* and *WS/AWC*. Much controversy surrounds the relationship between these two ratios, and the use of incorrect relationship in the model may lead to erroneous soil moisture estimates. To study this aspect, daily values of available moisture at Campina Grande are computed for 25 years using *Z* tables corresponding to the different curves of *Fig. 3*. The results are shown in *Fig. 4a* and *b*.

Table 1. Estimated soil water content (mm) exceeded at given probabilities

Probability	March–June			April–July			May–August		
Decade	25%	50%	75%	25%	50%	75%	25%	50%	75%
1	98	94	89	110	98	93	112	101	96
2	122	85	79	125	106	85	147	110	94
3	131	89	74	138	114	91	177	129	96
4	149	96	80	172	132	99	190	151	111
5	149	109	73	179	144	105	191	165	109
6	169	105	84	187	162	118	196	176	111
7	168	120	87	192	164	141	196	174	124
8	164	132	94	188	172	126	189	171	123
9	169	138	102	189	169	132	186	168	132
10	176	145	126	196	178	138	175	158	142
11	182	148	115	190	174	129	174	151	125
12	187	144	104	187	166	146	175	142	121

Station: Campina Grande Available water capacity: 200 mm

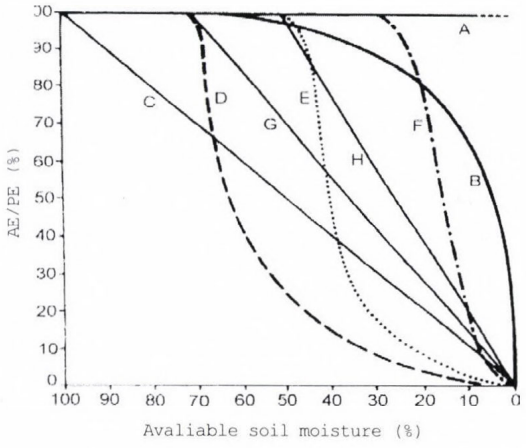

Fig. 3. Relationship between *AE/PE* and available soil moisture content (*Baier* and *Robertson*, 1966).

The lowest values of moisture content are observed when curve A is used in the model. This curve is based on the assumption, that moisture is equally available to plants for evapotranspiration over the range from field capacity to the permanent wilting point. According to *Baier et al.* (1979), this assumption is probably valid for sandy soils well permeated with roots.

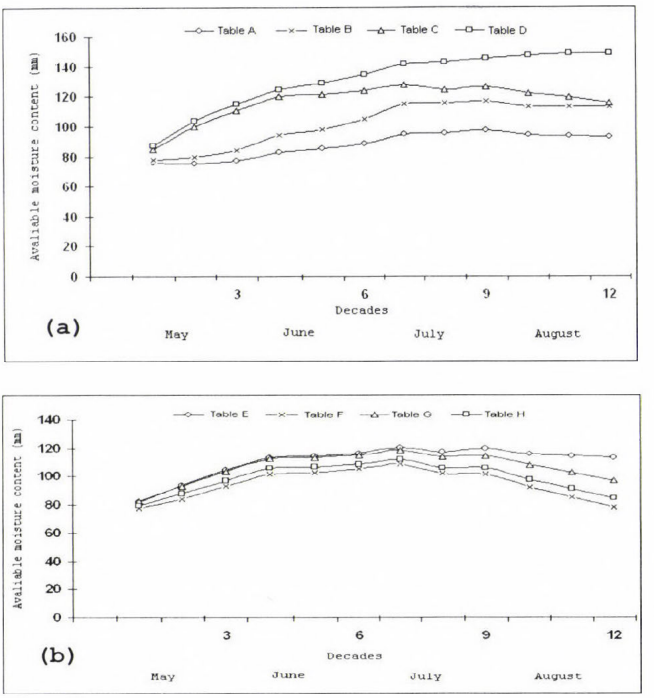

Fig. 4. Available soil moisture at Campina Grande based on different *Z* tables.

According to curve B, no significant decrease in evapotranspiration occurs except in very dry soil. This concept was suggested by *Pierce* (1958) and was used by *Gardner* (1960) for a sandy soil. Curve C assumes a linear relationship between the *AE/PE* ratio and the soil moisture percentage. Such a relation was supported by various authors (*Denmead* and *Shaw*, 1962; *Gardner* and *Ehlig*, 1963; *Smith*, 1959). Curves D, E, and F assume no reduction in the *AE/PE* ratio over the range of available moisture from 100 to 70% (curve D), to 50% (curve E), and to 30% (curve F). Beyond these limits the *AE/PE* ratio decreases rapidly with the drying of the soil. Curve G assumes no reduction in *AE/PE* over the range from 100 to 70% of available moisture and a linear decrease below 70%. This curve is recommended for most medium textured non-irrigated soils. Curve H is similar to curve G, except that no reduction in *AE/PE* ratio is assumed over the range from 100 to 50% of available soil moisture.

Soil moisture estimates based on curves B and E are quite similar, while the highest values of soil moisture are obtained with the use of curve D. Soil moisture values based on curves E, F, G, and H are very close to each other

over a large part of the four-month growing period. The results based on curve C are quite close to those obtained from all other curves except curve A. This is in agreement with *Baier*'s (1969) suggestion, that if soil moisture observations are not available for comparison, curve C provides a reasonable approximation.

If daily precipitation data over a long time period is not available, mean daily precipitation values derived from climatic monthly mean values can perhaps be used in the VSMB model to obtain an estimate of actual evapotranspiration. This aspect is studied using data for Campina Grande. *Brook*'s (1943) sine curve interpolation technique is used to derive daily precipitation values from climatic monthly means, and the resulting daily values are used together with the daily *PE* values to obtain daily values of *AE* during the growing season. From the 122 daily values, mean values for each decade are derived. These values are compared with mean decadal *AE* values obtained from the use of actual daily precipitation data for 25 years in the model (*Fig. 5*). Actual evapotranspiration obtained using mean daily precipitation data is always higher than that based on daily precipitation data. Use of mean precipitation data also shows the surface soil layers wetter and water surplus lower than in the case of using daily precipitation data. Actual evapotranspiration during the crop-growing season is an important parameter, and the close agreement between the two curves is quite encouraging.

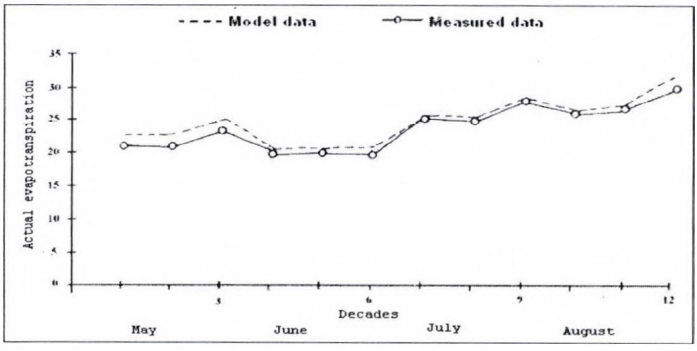

Fig. 5. Actual evapotranspiration (mm/decade) at Campina Grande obtained from the VSMB model using (1) mean daily precipitation data and (2) actual precipitation data.

Results of irrigation computations for Fortaleza for a limiting moisture value (*VC*) of 105 mm are given in *Table 2*. A summary of the results for all the stations is presented in *Table 3*.

As it is expected, the number of irrigations increases and the mean interval between irrigations decreases as the limiting moisture level increases. However, the change in the total water need is not very pronounced, since at higher *VC* values less water is applied in each irrigation. Comparison of water surplus data under irrigated and unirrigated conditions shows that, in general, the fraction of irrigation water that is lost as water surplus increases as the limiting moisture level increases.

Table 2. Irrigation requirements at Fortaleza.
$AWC = 150$ mm, $VC = 105$ mm. Period: April–July

Year	Number of irrigations	Mean interval between irrigations (days)	Number of days with available moisture content (mm) between		
			105–120	120–135	135–150
25	6	22	29	40	53
26	5	28	26	36	60
27	5	29	25	38	59
28	7	19	32	40	50
29	5	28	21	31	70
30	4	37	33	35	54
31	6	22	28	43	51
32	8	17	39	51	32
33	6	23	30	35	57
34	6	24	21	19	82
35	4	38	16	26	80
36	7	19	38	35	49
37	4	40	19	28	75
38	4	40	20	41	61
39	5	26	26	37	59
40	4	37	13	29	80
41	7	19	35	50	37
42	7	20	44	39	39
43	7	19	37	34	51
44	6	22	24	30	68
45	3	58	8	24	90
46	5	28	23	37	62
47	5	29	26	28	68
48	3	59	24	36	62
49	5	30	17	21	84
50	6	23	27	24	71
51	5	30	37	37	48
52	6	23	28	34	60
53	6	23	21	39	62
54	6	24	29	29	64
55	6	23	26	33	63
56	7	19	31	50	41
57	7	19	35	35	52

Table 3. Irrigation needs at the stations. $AWC = 150$ mm

Station	Crop growing period	Limiting soil moisture level (mm)	Number of irrigations	Mean interval between irrigations (days)	Irrigation amount (mm)
Iguatu	Mar – Jun	75	2	90	135
		105	4	37	150
		135	25	5	190
Fortaleza	Apr – Jul	75	3	74	200
		105	5	28	190
		135	29	5	220
Quixeramobim	Apr – Jul	75	3	55	200
		105	7	20	260
		135	37	3	280
São Gonçalo	Feb – May	75	2	94	135
		105	4	41	150
		135	27	5	200
Umbuzeiro	Jun – Sep	75	2	106	135
		105	3	72	110
		135	16	9	120
Campina Grande	May – Aug	75	1	116	70
		105	2	78	75
		135	13	10	100

The climatic water balance table for Sao Gonçalo based on Thornthwaite's procedure (*Thornthwaite* and *Mather*, 1957) for AWC value of 250 mm indicates the following values for the period February–May: PE = 507 mm, AE = 499 mm, P = 678 mm. It may be mentioned here, that this procedure is based on the relationship between *AE/PE* and *WS/AWC* given by curve C of *Fig. 3.*

Table 4. Potential evapotranspiration (*PE*), actual evapotranspiration (*AE*), and precipitation (*P*) during the growing periods based on Thornthwaite's procedure

Station	Campina Grande	Umbuzeiro	Iguatu	Fortaleza	Quixeramobim	São Gonçalo
Period	May – Aug	Jun – Sep	Mar – Jun	Apr – Jul	Apr – Jul	Feb – May
PE	304	284	492	511	543	507
AE	294	261	403	492	344	499
P	367	317	465	668	331	679

Results of the present study show, however, that even to maintain the moisture content above 50% of *AWC* irrigation is needed in each year of the 36-year study period. Comparison of data presented in *Table 4* with irrigation

needs at the stations (*Table 3*) indicates, that climatic water balance data may not be of much use in evaluating the agricultural potential of a region. Irrigation needs are evaluated at Campina Grande for *AWC* values of 100 and 200 mm and a *VC* level of 85%. The results show that to maintain similar moisture levels in the soil, more irrigation is necessary in the case of AWC_{100} than for AWC_{200}. Similar result was reported by *De Jong* (1985).

References

Allen, R.G., Pereira, L.S., Raes, D., and *Smith, M.*, 1998: Crop evapotranspiration. Guidelines for computing crop water requirements. *FAO Irrigation and drainage paper 56*. FAO, Rome, Italy. 301 pp.

Baier, W., 1969: Concepts of soil moisture availability and their effects on soil moisture estimates from a meteorological budget. *Agr. Meteorol. 6*, 165-178.

Baier, W. and *Robertson, G.W.*, 1966: A new versatile soil moisture budget. *Can J. Plant Sci. 46*, 299-315.

Baier, W., Dyer, J.A., and *Sharp, W.R.*, 1979: The versatile soil moisture budget. *Tech. Bull. 87*, Agrometeorology Section, Research Branch, Agriculture Canada, Ottawa, Ont. 52 pp.

Baier, W. and *Bootsma, A.*, 1999: Climate input requirements of soil-crop-weather models for climate change assessments. Agriculture and Agri-Food Canada, Research Branch, Eastern Cereal and Oilseed Research Center contribution No 981348,*Tech. Bull.* 33 pp.

Boisvert, J.B., Dyer, J.A., Lagace, R., and *Dube, P.A.*, 1992: Estimating water table fluctuations with a daily weather-based water budget approach. *Can. Agr. Eng. 34*, 115-124.

Brooks, C.E.P., 1943: Interpolation tables for daily values of meteorological elements. *Q. J. Roy. Meteor. Soc. 69*, 160-162.

Denmead, O.T. and *Shaw, R.H.*, 1962: Availability of soil water to plants as affected by soil moisture content and meteorological conditions. *Agron. J. 54*, 385-390.

De Jong, R., 1985: Soil water modelling using daily and mean daily data derived from historical monthly values. *Atmos.-Ocean 23*, 254-266.

De Jong, R., 1988: Comparison of two-soil water models under semi-arid growing conditions. *Can. J. Soil.Sci. 68*, 307-321.

De Jong, R. and *Bootsma, A.*, 1996: Review of recent developments in soil water simulation models. *Can. J. Soil. Sci. 76*, 263-273.

De Jong, R. and *Shaykewich, C.F.*, 1981: A soil water budget model with a nearly impermeable layer. *Can. J. Soil. Sci. 61*, 361-371.

De Jong, R., Bootsma, A., Dumanski, J., and *Samuel, K.*, 1992: Characterizing the soil water regime of the Canadian prairies. *Tech. Bull. 1992-2E*. Center for Land and Biological Research, Agriculture Canada. Ottawa, ON, 15 pp.

Doorenbos, J. and *Kassam, A.H.*, 1979: Yield response to water. *FAO Irrigation and Drainage Paper*, No. 33. FAO, Rome, Italy. 193 pp.

Doorenbos, J. and *Pruitt, W.O.*, 1977: Guidelines for prediction of crop water requirements. *FAO Irrigation and Drainage Paper*, No. 24. FAO, Rome, Italy. 156 pp.

Dyer, J.A. and *De Jager, J.M.*, 1986: Assessment of recent drought severity for natural grassland at three locations. *S.A.J. Plant. Sci. 3*, 80-82.

Dyer, J.A. and *Mack, A.R.*, 1984:Tthe versatile soil moisture budget – version three. *LRRI Contribution No. 82-3*, Agriculture Canada, Ottawa, Ontario, Canada, 24 pp.

Gardner, W.R., 1960: Dynamic aspects of water availability to plants. *Soil Sci. 89*, 63-73.

Gardner, W.R. and *Ehlig, C.F.*, 1963: The influence of soil water on transpiration by plants. *J. Geophys. Res. 68*, 5719-5724.

Holmes, R.M., and *Robertson, G.W.*, 1959: A modulated soil moisture budget. *Mon. Weather Rev. 87*, 101-106.

Pierce, L.T., 1958: Estimating seasonal and short-term fluctuations in evapotranspiration from meadow crops. *B. Am. Meteorol. Soc. 39*, 73-78.

Robertson, G.W., 1977: A versatile soil moisture budget for drought prone regions and dryland farming areas in India. Prepared as part of *FAO/TF/IND/136*. Drought prone areas project. Dryland Agriculture Center, Hyderabad 500012, India, 50 pp.

Robertson, G.W., 1985: Multiple-crop multiple-layer soil-water budget: *A computer program documentation*. Supply and Services Canada. Ottawa. 41 pp.

Robertson, G.W. and *Foong, Sang Foo*, 1977: Weather based yield forecast for oil palm fresh fruit bunches. *Proc. of the Malaysian International Oil Palm Conference, 1976*. The Incorporated Society of Planters, 695-709.

Smith, G.W., 1959: The determination of soil moisture under a permanent grass cover. *J. Geophys. Res. 64*, 477-483.

Thornthwaite, C.W., 1948: An approach toward a rational classification of climate. *Geogr. Rev. 38*, 55-94.

Thornthwaite, C.W. and *Mather, J.R.*, 1955: The water balance. *Publ. Climatol. 8* (1). Lab of Climatology. N.J., 1-104.

Thornthwaite, C.W. and *Mather, J.R.*, 1957: Instructions and tables for computing potential evapotranspiration and the water balance. *Publ. Climatol. 10* (3). Lab of Climatology. N.J., 185-311.

GUIDE FOR AUTHORS OF *IDŐJÁRÁS*

The purpose of the journal is to publish papers in any field of meteorology and atmosphere related scientific areas. These may be

- research papers on new results of scientific investigations,
- critical review articles summarizing the current state of art of a certain topic,
- short contributions dealing with a particular question.

Some issues contain "News" and "Book review", therefore, such contributions are also welcome. The papers must be in American English and should be checked by a native speaker if necessary.

Authors are requested to send their manuscripts to

Editor-in Chief of IDŐJÁRÁS

P.O. Box 39, H-1675 Budapest, Hungary

in three identical printed copies including all illustrations. Papers will then be reviewed normally by two independent referees, who remain unidentified for the author(s). The Editor-in-Chief will inform the author(s) whether or not the paper is acceptable for publication, and what modifications, if any, are necessary.

Please, follow the order given below when typing manuscripts.

Title part: should consist of the title, the name(s) of the author(s), their affiliation(s) including full postal and e-mail address(es). In case of more than one author, the corresponding author must be identified.

Abstract: should contain the purpose, the applied data and methods as well as the basic conclusion(s) of the paper.

Key-words: must be included (from 5 to 10) to help to classify the topic.

Text: has to be typed in single spacing with wide margins on one side of an A4 size white paper. Use of S.I. units are expected, and the use of negative exponent is preferred to fractional sign. Mathematical formulae are expected to be as simple as possible and numbered in parentheses at the right margin.

All publications cited in the text should be presented in a *list of references*, arranged in alphabetical order. For an article: name(s) of author(s) in Italics, year, title of article, name of journal, volume, number (the latter two in Italics) and pages. E.g., *Nathan, K.K.,* 1986: A note on the relationship between photo-synthetically active radiation and cloud amount. *Időjárás 90,* 10-13. For a book: name(s) of author(s), year, title of the book (all in Italics except the year), publisher and place of publication. E.g., *Junge, C.E.,* 1963: *Air Chemistry and Radioactivity*. Academic Press, New York and London. Reference in the text should contain the name(s) of the author(s) in Italics and year of publication. E.g., in the case of one author: *Miller* (1989); in the case of two authors: *Gamov* and *Cleveland* (1973); and if there are more than two authors: *Smith et al.* (1990). If the name of the author cannot be fitted into the text: *(Miller,* 1989); etc. When referring papers published in the same year by the same author, letters a, b, c, etc. should follow the year of publication.

Tables should be marked by Arabic numbers and printed in separate sheets with their numbers and legends given below them. Avoid too lengthy or complicated tables, or tables duplicating results given in other form in the manuscript (e.g., graphs)

Figures should also be marked with Arabic numbers and printed in black and white in camera-ready form in separate sheets with their numbers and captions given below them. JPG, GIF, or XLS formats should be used for electronic artwork submission.

The text should be submitted both in manuscript and in electronic form, the latter on disks or in e-mail. Use standard 3.5" MS-DOS formatted diskette or CD for this purpose. MS Word format is preferred.

Reprints: authors receive 30 reprints free of charge. Additional reprints may be ordered at the authors' expense when sending back the proofs to the Editorial Office.

Information on the last issues: http://www.met.hu/Journal-Idojaras.php

Published by the Hungarian Meteorological Service

Budapest, Hungary

INDEX: 26 361

HU ISSN 0324-6329